Solar Energy 301 (2025) 113961

Contents lists available at ScienceDirect

Solar Energy

journal homepage: www.elsevier.com/locate/solener

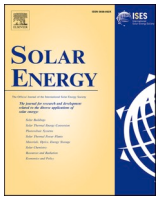

Microstructural stability of coatings with high solar absorptance for ceramic particles during thermocyclic exposure for concentrated solar thermal applications

C. Oskay [a,*], M. Bik [b,*], C. Grimme [a], E. White [a], S. Auler [a], M. Kerbstadt [a], G. Alkan [c], P. Mechnich [c], G. San Vicente [d], A. Morales [d], F. Sutter [e], D. Benitez [e], A.C. González Alves [e], N. Benameur [f], S. Merlin [f], M. Galetz [a]

[a] DECHEMA-Forschungsinstitut, Theodor-Heuss-Allee 25, 60486 Frankfurt (Main), Germany
[b] AGH University of Krakow, al. Mickiewicza 30/B8 3.12, 30-059 Krakow, Poland
[c] German Aerospace Center DLR, Institute of Materials Research, Linder Höhe, 51147 Cologne, Germany
[d] CIEMAT-PSA, Avenida Complutense 40, E28040 Madrid, Spain
[e] German Aerospace Center DLR, Institute of Solar Research, Calle Doctor Carracido Nr. 44, 1st floor, 04005 Almería, Spain
[f] Saint-Gobain Research Provence, Avenue Alphonse Jauffret 550, CS 20224 – F 84306 Cavaillon Cedex, France

ARTICLE INFO

Keywords:
CST technology
Ceramic particles
Spinel-based coatings
Optical properties
Thermocyclic exposure
Interdiffusion

ABSTRACT

Spinel-based coatings were deposited on Fe_2O_3-rich ceramic particles to investigate their microstructural stability and optical properties during thermocyclic oxidation at 1000 °C for up to 3000 h. The solar absorptance over time remained stable at a very high level (around 97 %) for the Cu-Cr and Cu-Mn-Co spinel coatings, whereas the Cu-Mn-Fe spinel coating showed a significant increase in its solar absorptance during early stages of exposure and thereafter maintained a stable behavior around 95 %. The microstructural investigations, coupling EPMA analysis with phase mapping via Raman spectroscopy, revealed the formation of complex microstructures consisting of different spinel phases for the coatings due to high temperature interdiffusion between the spinels and the substrate, respectively. Such exchange reactions continued during thermocyclic exposure, but they did not affect the highly promising long-term solar absorptance of the coatings for particle-based CST applications.

1. Introduction

In recent years concentrated solar thermal (CST) technologies have emerged as an efficient and climate-neutral method to generate electricity. Coupling the concentrated solar power with thermal energy storage offers a vast potential for flexibility. Due to their ideal thermal and physical properties and low cost, the application of nitrate salts has prevailed in commercial projects [1,2]. Other salt mixtures, such as ternary carbonates and chlorides with higher possible operating temperatures, have been investigated as potential candidates [3]. The increase in operating temperatures through their use is highly promising, since the operation of a power block with a Brayton sCO_2 cycle with higher efficiency could be achieved [4]. However, the price of carbonates [5] and the high corrosivity of the chlorides [6] have restricted their commercial use so far.

An innovative solar particle receiver concept was developed by the U.S. Department of Energy's Sandia National Laboratories in the 1980 s [7], where ceramic particles were suggested as a viable alternative to increase the operating temperatures of next-generation CST plants. A further advantage of solid particles for heat transfer and storage is the absence of freeze–thaw effects occurring in molten salts during cyclic operation.

Solar particle-based CST technology uses ceramic particles as a combined absorber and transfer medium, which are transported to the receiver, where they are heated up to temperatures around 1000 °C using concentrated solar irradiation [8]. Thereafter, the heated particles can be stored or directly transported into a heat exchanger, where they transfer the thermal energy to generate supercritical CO_2 at temperatures around 700 °C and pressures around 20 MPa which drives a Brayton power cycle with significantly improved thermal efficiencies of around 50 % [9,10]. Further details on solar particle receivers can be found in [11].

* Corresponding authors.
E-mail addresses: ceyhun.oskay@dechema.de (C. Oskay), mbik@agh.edu.pl (M. Bik).

https://doi.org/10.1016/j.solener.2025.113961
Received 11 July 2025; Received in revised form 22 August 2025; Accepted 4 September 2025
Available online 15 September 2025

Table 1
Chemical composition and application-relevant properties of the substrate particles used in this study from [19].

Chemical composition [wt. %]		Solar absorptance	Thermal emittance	Bulk density [g/cm^3]	Breaking force [N]	Specific heat capacity at 1000 °C [J/gK]	Cost/kg [EUR]
Al_2O_3	> 30 wt%	0.833	0.614	2.0	120–140	1.1	≈ 1.0
Fe_2O_3	< 30 wt%						
SiO_2	< 20 wt%						
ZrO_2	> 20 wt%						
others	≈ 5 wt%						

Various solid particles have been investigated as the heat transfer medium for next-generation power plants, mainly based on their applicability, cost, mechanical properties, and optical behavior. Ideally, the ceramic particles should possess high solar absorptance and high heat capacity coupled with sufficient mechanical strength, low thermal emittance, and all at a low cost [8,12–14]. The most prominent candidate is the sintered-bauxite and its variants, which are widely used in the fracking industry as the so-called "proppants" [15]. Sintered-bauxite proppants fulfill most of the above-stated properties satisfactorily, with one exception: sustained high solar absorptance over time. They generally consist of Al_2O_3, SiO_2, TiO_2 and Fe_2O_3 in varying molar ratios [13,16]. While offering high mechanical strength at the application-relevant temperatures [16] together with high solar absorptance around 90 % in the as-received condition [13], they exhibit a substantial deterioration of solar absorptance within the early stages of exposure at high temperatures [14]. This degradation was predominantly associated with the formation of Fe-containing complex oxides such as Fe_2TiO_5 and $FeAlTiO_5$ during exposure in oxidizing atmospheres [13,17]. In line with other studies from the literature [14,18], an average reduction of approximately 14 % was observed in a recent investigation for the solar absorptance of four different proppants within the first 500 h of isothermal exposure in still air at 1000 °C [19].

Besides sintered-bauxite proppants, other candidates such as black SiC have been investigated. Despite maintaining a high solar absorptance exceeding 90 % and exhibiting high phase stability even after ageing tests in air at 900 °C [20], the high cost of this synthetic material limits its application as heat transfer media [14]. In contrast, a high cost-efficiency can be achieved by the utilization of natural granular materials such as quartz sand or secondary raw materials such as metallurgical slags. For quartz, despite the low price, its α→β phase transformation and the associated volume changes at 573 °C restrict its utilization [12]. For the metallurgical slags, despite promising optical, thermal and mechanical properties, the frequently silica-rich compositions can be a limiting factor for high temperature use [21].

Coatings with high solar absorptance have been widely investigated for the receiver panels of current molten salt-based power plants. Usually, such coatings can be divided into two categories: (i) solar selective coatings, or (ii) non-selective coatings utilizing black pigments. Solar selective coatings combine high absorptance with a very low emissivity; however, they consist of several layers [22]. Hence, their application usually involves complex manufacturing methods such as magnetron sputtering [23]. On the other hand, non-selective coatings usually focus on a high absorptance achieved by a simpler manufacturing method, such as slurry deposition, dip coating or painting [24]. Both categories enable a high opto-thermal efficiency, increasing the thermal energy input to the system, while the easier manufacturing methods and the consequential cost-effectiveness for non-selective coatings, facilitates their industrial use [25]. The commercialization of the paint "PYROMARK 2500" and the investigation of its optical properties and degradation mechanisms [26,27] paved the way for the investigation of different formulations including spinel-based black pigments with the general AB_2O_4 structure (A and B: transition metals such as Cu, Cr, Co, Mn, Fe with partially filled d orbitals) dispersed in a silica matrix [28–30]. Such coatings on metallic substrates have been shown to improve the absorptance significantly. Their oxidation behavior and optical properties have been characterized extensively for application in the absorbers of molten salt-based systems [31–34].

Few studies can be found in the literature regarding the optical properties and degradation mechanisms of the spinel-based coatings with high solar absorptance deposited on ceramic particles. For instance, Cu-Cr-Mn and Cu-Cr spinel coatings significantly increased quartz sand absorptance during isothermal annealing at 800 °C [35]. Similarly, Gobereit et al. investigated the diffusion of transition metal cations into proppants by dip coating of PYROMARK 2500 followed by heat treatment and showed an improved solar absorptance from 87 % to 95 % [17]. Furthermore, Cu-Mn-Fe spinel coatings deposited onto bauxite proppants using resonance acoustic mixing (RAM), followed by a heat treatment at 1200 °C for 2 h, revealed a substantial improvement of the solar absorptance to 92 % [36]. In a similar manner, Co-Cu-Mn spinel-based coatings with and without the addition of silica nanoparticles were prepared using precursor solutions and deposited onto proppants by dip coating, followed by heat treatment. Such coatings increased the absorptance of proppants significantly and retained a high solar absorptance even after 4000 h of isothermal ageing at 1000 °C [19,37].

This study investigates the microstructural stability of three spinel-based coatings with high solar absorptance during thermocyclic exposure at 1000 °C. Starting from an in-depth characterization of the spinel phases in the as-deposited coatings, their solar-weighted absorptance as a function of exposure duration, and the detailed characterization of chemical and phase changes during 3000 h long-term cyclic operation are reported. The relevant performance aspects are described for particle-based CST applications.

2. Materials and methods

2.1. Particles and coatings

A previous study reported on the development of four Fe_2O_3-rich (compared to proppants) particle generations, manufactured by granulation of waste products from the steel industry [19]. The mechanical, thermal, and optical properties of particles were optimized in terms of their chemical composition among the different generations. In the current study, the fourth generation was selected as the substrate since these particles offered the best balance between mechanical stability and heat capacity at a low manufacturing cost (see Table 1, [19]). Since the optimization from mechanical and economical aspects led to a lower solar absorptance of such particles, different coatings were designed to enhance this critical property.

The investigated coatings included Cu-Mn-Fe spinel pigments deposited by high energy resonance acoustic mixing analogous to the study in [36] (hereafter referred to as DLR coating), Cu-Mn-Co spinel deposited by a dip coating-like process using a $CuCoMnO_x$ precursor solution with SiO_2 nanoparticles corresponding to the investigation in [37] (hereafter referred to as CIE coating) and Cu-Cr spinel pigments dispersed in a silica matrix deposited by a slurry deposition method, see [24] (hereafter referred to as DFI coating). The first two coatings were heat-treated for 2 h at 1200 °C and 1000 °C, respectively, whereas the DFI coating was cured at ambient temperature with a similar process as described in [38]. Further details on the substrate particles and the

Table 2
Manufacturing methods and application-relevant properties of the coated particles investigated in this study, from [19]. Please note that the cost estimations were conducted for coated particles, and the cost of the coatings was estimated based on raw material costs.

Coating	Spinel	Manufacturing method	Solar absorptance	Thermal emittance	Estimated cost/kg [EUR]
DLR	Cu-Mn-Fe	High energy resonance acoustic mixing followed by curing at 1200 °C	0.926	0.708	≈ 1.6
CIE	Cu-Mn-Co	Dip coating-like process using precursor solutions followed by curing at 1000 °C	0.967	0.809	≈ 1.6
DFI	Cu-Cr	Slurry deposition by followed by curing at ambient temperature	0.970	0.931	≈ 1.6

coating deposition methods can be found in [19]. All three coatings resulted in a significant improvement in the solar absorptance. The application-relevant properties of the coated particles are summarized in Table 2:

2.2. Thermocyclic exposure tests

Thermocyclic exposure tests of the coated particles were undertaken at 1000 °C with 3 h cycles up to a maximum hot dwell duration of 3000 h in a test rig equipped with an alumina furnace tube (Fig. 1). Approximately 10 g were filled in alumina crucibles and placed in the test rig. Temperature was controlled within ± 5 K using a type S thermocouple in the vicinity of the first crucible. Tests were performed following the standard ISO 13573:2012 [39]. Each cycle included a heating stage up to 97 % of the exposure temperature (in K, according to the standard) followed by 3 h of hot dwell and pressurized air cooling of the samples below 50 °C for 30 mins, which was enabled by slitting the furnace tube (see Fig. 1). The slit width was adapted according to the uniform temperature zone. Compressed air cooling was used to initiate very high cooling rates (average around 150 K/min) and to increase the build-up of thermally induced stresses in the coatings due to the mismatch of thermal expansion coefficients between different oxide phases. With this approach, information on the thermal shock resistance of the investigated coatings was obtained. After exposure, the coated particles were removed from the crucibles to enable optical and analytical characterization.

2.3. Optical and analytical characterization

The hemispherical reflectance (ρ_h) spectra of all coated particles were measured (one sample per condition) prior to and after thermocyclic exposure using a UV–VIS-NIR double-beam spectrophotometer (PerkinElmer Lambda 950) equipped with a Spectralon® coated 150 mm integrating sphere in the wavelength range between 300 – 2500 nm. The Montecchi window optical model was applied, as outlined in the SolarPACES reflectance guideline [40]. The solar-weighted absorptance (α_s) was calculated from the ρ_h spectra using the direct AM1.5 solar spectrum (ASTM G173-03) according to the ASTM standard E903-20 procedure [41]. Further details on the reflectance measurements and the derivation of the solar-weighted absorptance can be found in [37].

Microstructural and chemical analyses were performed on cross-sections of the coated particles. For this purpose, particle samples were hot mounted in commercially available epoxy resin using an advanced electro-hydraulic mounting press (Struers Cito-press 30, Denmark). Cross-sections were further prepared by metallographic methods, including wet automated grinding with progressively finer SiC paper up to 2400 grit and polishing using diamond suspensions down to a 1 μm finish.

Electron-probe microanalysis (EPMA, JEOL JXA-8100 with W-cathode) equipped with wavelength dispersive X-ray spectroscopy (WDX) was conducted to obtain high-resolution backscattered electron (BSE) images, elemental distribution maps and spot measurements to ascertain the chemical composition of selected spots in the coatings. Raman spectroscopy was used to determine the oxide phases in the coatings.

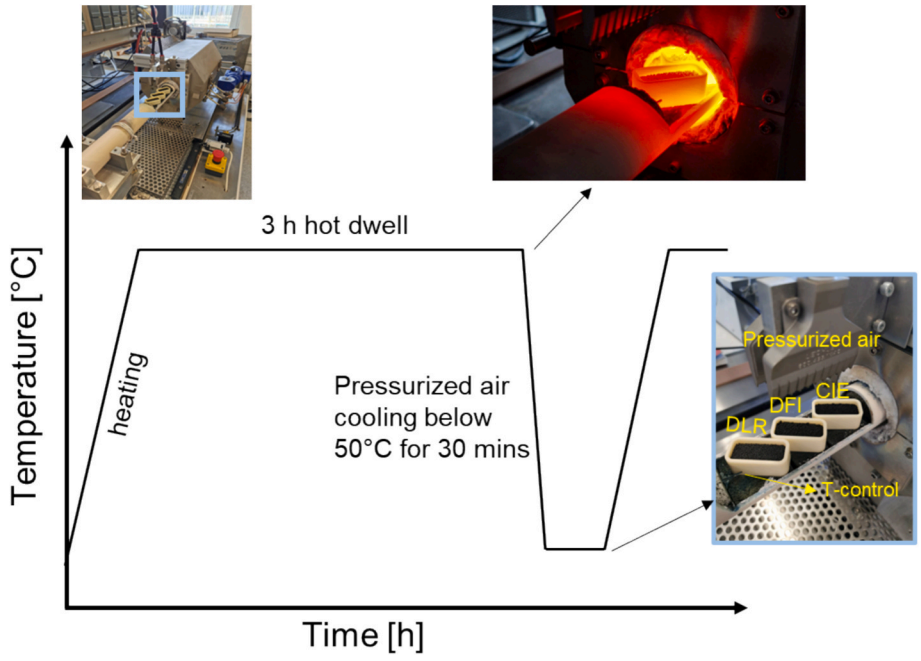

Fig. 1. Schematic temperature profile of the thermocyclic exposure showing the heating, hot and cold dwell stages of a cycle, and images of the furnace rig and coated particles in alumina crucibles at the end of the hot and cold dwell stages.

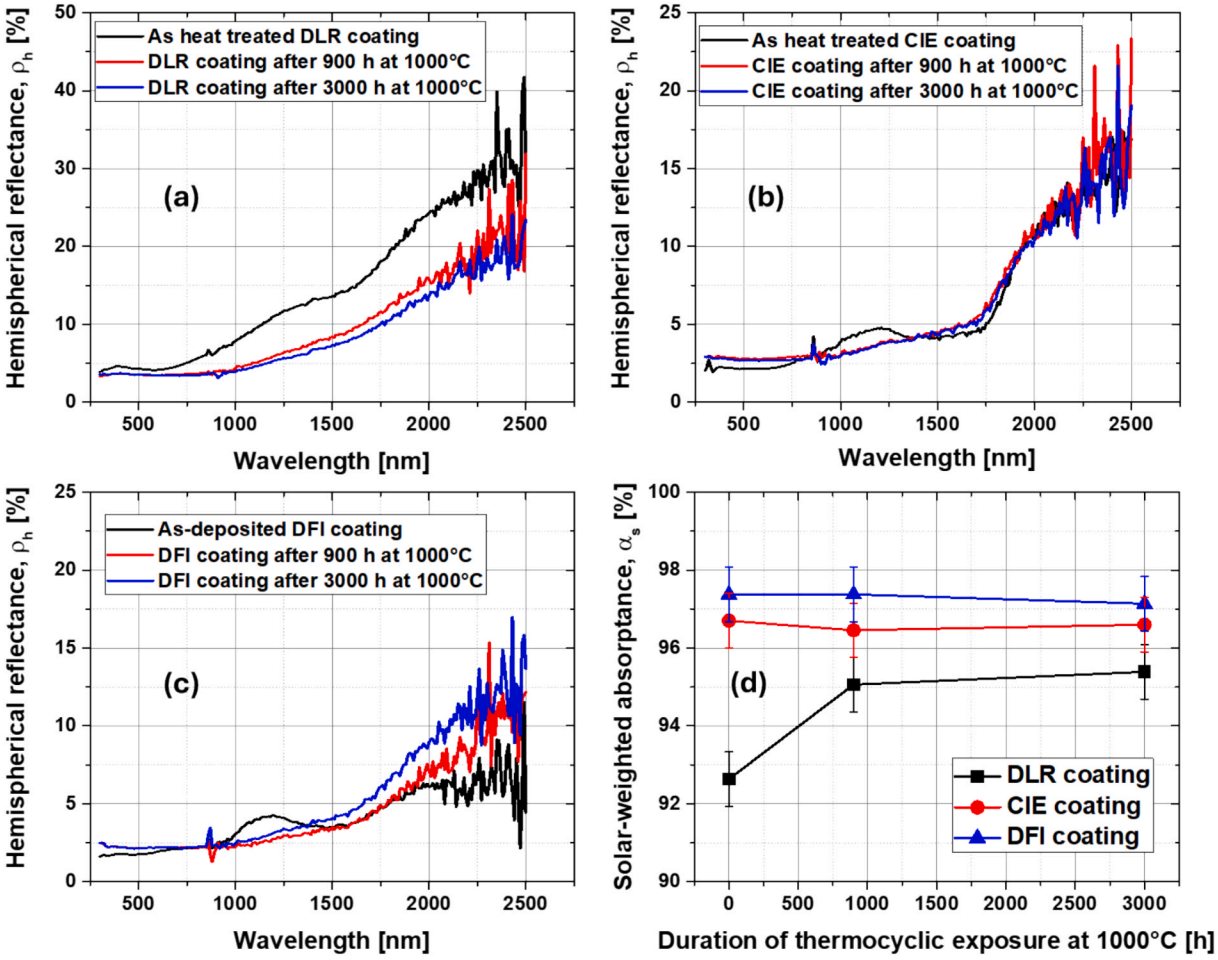

Fig. 2. Hemispherical reflectance spectra of (a) DLR, (b) CIE and (c) DFI coated particles in the as-deposited or heat-treated condition and after thermocyclic exposure at 1000 °C; (d) solar-weighted absorptance of investigated coatings as a function of thermocyclic exposure duration (error bars showing the measurement uncertainty originating from the repeatability of individual measurements (0.2 % in [42]) and 0.5 % from the calibration standard [41]). Please note the varying y-axis in the respective hemispherical spectra for coatings.

This was executed using a WITec alpha 300 M + spectrometer with a 488 nm laser (laser spot approx. 650 nm in diameter), 100x ZEISS Epiplan-Neufluar objective (NA = 0.9), 600 grating, and an Andor CCD detector. Mapping analyses were conducted on cross-sections within representative areas, and, more importantly, co-localized areas investigated with EPMA analysis beforehand. Areas chosen for Raman mapping were adjusted to accommodate the different thicknesses and compositions of the coatings. Due to the presence of alumina in the coated particles, two different regions were measured (50–4000 cm^{-1} and 4000–7000 cm^{-1}). Lateral resolution was always 500 nm in both the X and Y axes, and integration times were equal either to 3 s while recording spectra within 50–4000 cm^{-1} spectral region or 0.5 s for alumina investigation within the 4000–7000 cm^{-1} region. The laser power was adjusted to 1.5 mW. WITec Control FIVE software was used to collect Raman data and Witec Project FIVE 5.3, as well as OPUS 7.2. softwares were used to post-process data (cosmic spikes removal (the CRR filter) and extraction of the desired ranges of 115–1200 and 5000–7000 cm^{-1}. In the last step, the analysis of the recorded maps was done – the characteristic spectral regions (e.g. the 300 cm^{-1} α-Fe_2O_3 hematite band) were selected from post-processed spectra, and an integration filter (with a specific position and width on the spectrum) was applied, allowing selection of the compounds and precise generation of phase distribution maps. Subsequently, spectra corresponding to specific phases were chosen manually, and the combined distribution image (created from all distribution maps) was overlayed with confocal images and SEM images of the EPMA analyses.

3. Results

3.1. Optical characterization

Fig. 1 shows the ρ_h spectra of the coated particles prior to and after thermocyclic exposure at 1000 °C, together with the α_s values as a function of exposure duration. The DFI and CIE coatings exhibited comparable behavior both in the as-deposited and heat-treated conditions and after thermocyclic exposure. While showing a reflectance peak around 1200 nm in the initial condition, it disappeared during the test, decreasing their hemispherical reflectance in this region. Additionally, within the visible region and the near-infrared region (NIR), a slight increase in reflectance for both coatings over time was distinguished, especially at higher wavelengths. Unlike the other coatings, the heat-treated DLR coating showed higher reflectance in the visible and NIR region of the spectrum compared to others. In contrast, after 900 h of thermocyclic exposure, these comparatively high reflectance values in the visible and NIR region for the heat-treated DLR coating decreased to a similar level as other coatings. Compared to the α_s values of uncoated particles around 83 % in the as-received condition (see Table 1), all three investigated coatings led to a significant increase in the solar absorptance. The increase was around 16.5 % for the DFI coating, 16.1 % for the CIE coating, and 11.2 % for the DLR coating. While the DFI and CIE coatings maintained their high absorptance around 97 % even after 3000 h of thermocyclic exposure, the DLR coating showed a notable increase within the first 900 h of exposure, followed by a comparable

Table 3
Elemental concentrations determined using EPMA spot measurements by WDX from representative spots shown in Fig. 2. Please note that the measured area can be larger than the spot shown and therefore the influence of the surrounding phases cannot be excluded and elements with very low concentration originating from coating and/or substrate additives have not been shown for better clarity. This information is also valid for the upcoming tables.

Coating	aSpot no.	Concentration (at.%)							
		Fe	Mn	Cu	Al	Si	Cr	Co	O
DLR	1	21.7	5.8	9.0	8.3	0.6	–	–	52.5
	2	17.9	4.9	7.6	8.7	1.7	–	–	55.9
	3	20.3	5.3	6.0	9.2	0.6	–	–	55.3
CIE	1	19.0	8.4	5.6	2.1	2.5	–	4.3	56.8
	2	22.7	2.9	8.1	5.1	2.5	–	0.7	56.9
	3	17.3	4.6	7.6	9.7	0.8	–	2.7	54.5
DFI	1	3.0	–	2.2	1.0	11.9	25.3	–	53.6
	2	5.5	–	7.3	1.4	16.5	14.1	–	52.4

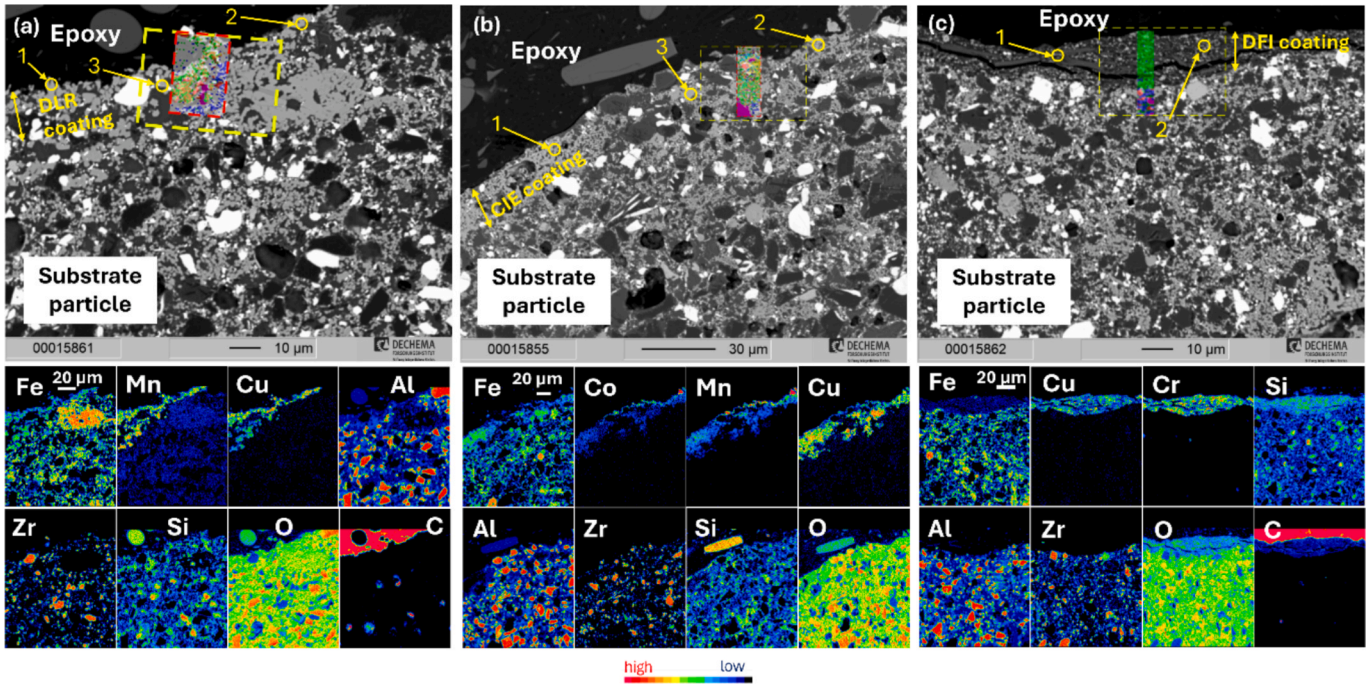

Fig. 3. Cross-sectional BSE images of (a) DLR, (b) CIE, and (c) DFI coatings as-deposited on substrate particles. Yellow circles indicate representative spots selected for WDX compositional analysis (shown in Table 3). The regions used for co-localized Raman confocal imaging (dashed yellow frame) and Raman mapping (red dashed frame, embedded within the yellow frame in (b) and (c)) are also shown. Corresponding EPMA elemental distribution maps are displayed below each BSE image. Please note the varying magnifications across the images. The DLR and CIE coatings were heat-treated, while the DFI coating was dried at ambient temperature without heat treatment.

stable trend for progressing exposure for up to 3000 h. It should be noted that the uncoated particles could not be included in the exposure tests due to space restrictions, however their rather stable optical behavior during isothermal exposure, unlike proppants, has been reported elsewhere [19].

3.2. *Microstructure of as-deposited coatings*

Fig. 2 illustrates the cross-sectional BSE images and EPMA elemental distribution maps of the investigated coatings in the initial as-deposited (for the DFI coating) and heat-treated conditions (CIE and DLR coatings). The thickness of the investigated coatings varied between 10–20 µm. The enrichment of constituting cations of the utilized coating spinel phases (see Table 2) was observed: for the DLR coating Fe, Mn, and Cu, for the CIE coating Co, Mn, and Cu, and for the DFI coating Cu and Cr are enriched at the surface. Moreover, significant Fe- and Al-enrichment can be detected in the CIE and DLR coatings, respectively (see Table 3), even though the initial coating spinel phases do not include these elements. The DFI coating, which is not exposed to high temperatures during manufacturing, explicitly consisted of "pristine" Cu-Cr spinel dispersed in a silica matrix.

While the determination of the chemical compositions from representative spots provided preliminary information on the enrichment of elements from the substrate particles within the DLR and CIE coatings due to heat-treatment, the determination of spinel phases with high solar absorptance was necessary to obtain a better understanding of the chemical interaction between the substrate and the coating. Fig. 3 depicts the phase mapping of the DLR coated particles using Raman spectroscopy. Two different phases can be differentiated with Raman imaging. The first, most dominant coating component, present across the entire mapped area, is mainly based on Al-enriched $CuFe_2O_4$ spinel – it is represented by a distinguished spectrum with five bands (approx. 180, 332, 485, 700 and 716 cm^{-1}). The first four bands with 700 cm^{-1} as the most characteristic strongly suggest the presence of $CuFe_2O_4$ [43,44], whereas the high half-band width of the $A_{1(g)}$ band with another maximum shifted significantly above 700 (716 cm^{-1}) indicate the enrichment of Al^{3+} cations that probably diffuse from neighboring α-Al_2O_3 (bands at around 6061 and 6091 cm^{-1} [45]) and form AlO_6

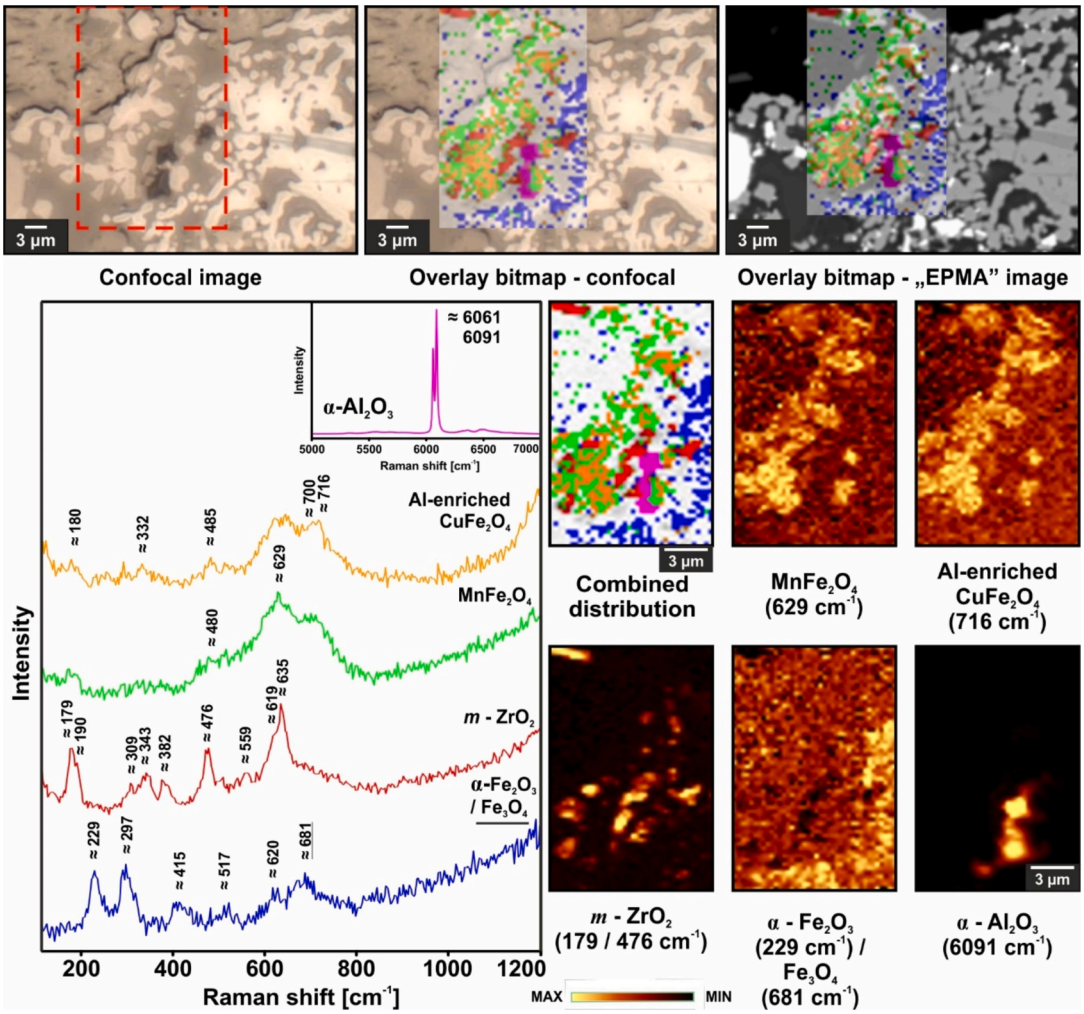

Fig. 4. Raman confocal imaging of DLR coating after heat-treatment. The following information applies to all further images concerning Raman imaging – the red square in the confocal images corresponds to the area investigated with Raman. Distribution images of phases (based on the integration of the most characteristic bands with their Raman shift given in the brackets) are presented with corresponding spectra. Spectra are noted with bands characteristic for particular phases. For α-Fe_2O_3 and Fe_3O_4 it was not possible to differentiate between them as the signal from Fe_3O_4 was too low for its integration, but its main band is still visible in the spectrum, which suggests its coexistence within the same area. Therefore, some band positions and corresponding phases are underlined.

octahedral units [46] during the curing stage. Since $FeAl_2O_4$ spinel shows an $A_{1(g)}$ main band at much higher Raman shift values [47], the region marked with orange in the overlay distribution is probably composed of Al-enriched $CuFe_2O_4$ spinel. Both, AlO_6 and FeO_6 octahedral units reveal one broad band with barely visible maxima due to so-called one-mode behavior [46]. For the second coating component, also present within the whole coating, but especially in the bottom part, two bands in the recorded Raman spectra (480 and 629 cm^{-1} as the most characteristic) can be assigned to $MnFe_2O_4$ spinel [48]. It should be noted that one cannot exclude the presence of either spinel variant in both described regions; it is rather a mixture of Al-enriched $CuFe_2O_4$ dominating in the upper part and $MnFe_2O_4$ in the bottom part. Such results are in perfect agreement with the EPMA mapping analysis (see Fig. 2.a) and point measurements showing a higher Cu/Mn ratio near the surface of the coating than at the coating/particle interface (compare spots 1 and 2 with 3 for the DLR coating in Table 3). Considering the starting composition of the coating ($CuFeMnO_x$), such results strongly suggest diffusion within the coating, as well as strong diffusion (especially Fe^{2+}/Fe^{3+} and $Al^{3+)}$ from the ceramic particles during curing. Underneath the coating, besides the aforementioned α-Al_2O_3, the phase mapping of the substrate particles showed monoclinic ZrO_2 (*m*-ZrO_2) based on numerous bands with the most characteristic doublet at ca. 179 and 190 cm^{-1} and another band at approx. 476 cm^{-1} [49], as well as mixture of hematite α-Fe_2O_3 (bands approx. 229, 297 – the most characteristic, 415, 517 and 620 cm^{-1} [50]) and a very low share of magnetite Fe_3O_4 (the main band at approx. 681 cm^{-1} of low intensity as compared to hematite bands [50]). These findings for ceramic particles are consistent for the following coated systems.

The microstructure of the heat-treated CIE coating (see Fig. 4) is more complex than for the DLR coating. Bands in the Raman spectra recorded within the top part (approx. 479 and 638 cm^{-1} as the most characteristic) can be assigned to $CoMn_2O_4$ spinel [51,52], which is in line with the colocalized EPMA mapping analysis (Fig. 2.b) and representative spot measurements (see spot 1 for the CIE coating in Table 3) demonstrating the increased concentration of Co and Mn in the 2–3 µm thick top layer. Underneath this top layer, a slightly thicker region (7–8 µm) consisting of Al-enriched $CuFe_2O_4$ spinel can be identified. Regarding the Al-enrichment in this spinel, a similar explanation (Al diffusion during the curing from particles) and band attribution (one-mode behavior) can be given, analogous to the DLR coating [43,44,46]. Three more coating constituents could be detected: $MnCo_2O_4$, $MnFe_2O_4$ and $CuFe_2O_4$. They are represented by the corresponding spectra with: four bands (172, 478, 508 and 650 cm^{-1} as the most characteristic) originating from $MnCo_2O_4$ [53], two bands (476 and 610 cm^{-1} as the most characteristic) from $MnFe_2O_4$ [48], and another four (175, 350, 485 and 702 cm^{-1} as the most characteristic) from $CuFe_2O_4$ spinel

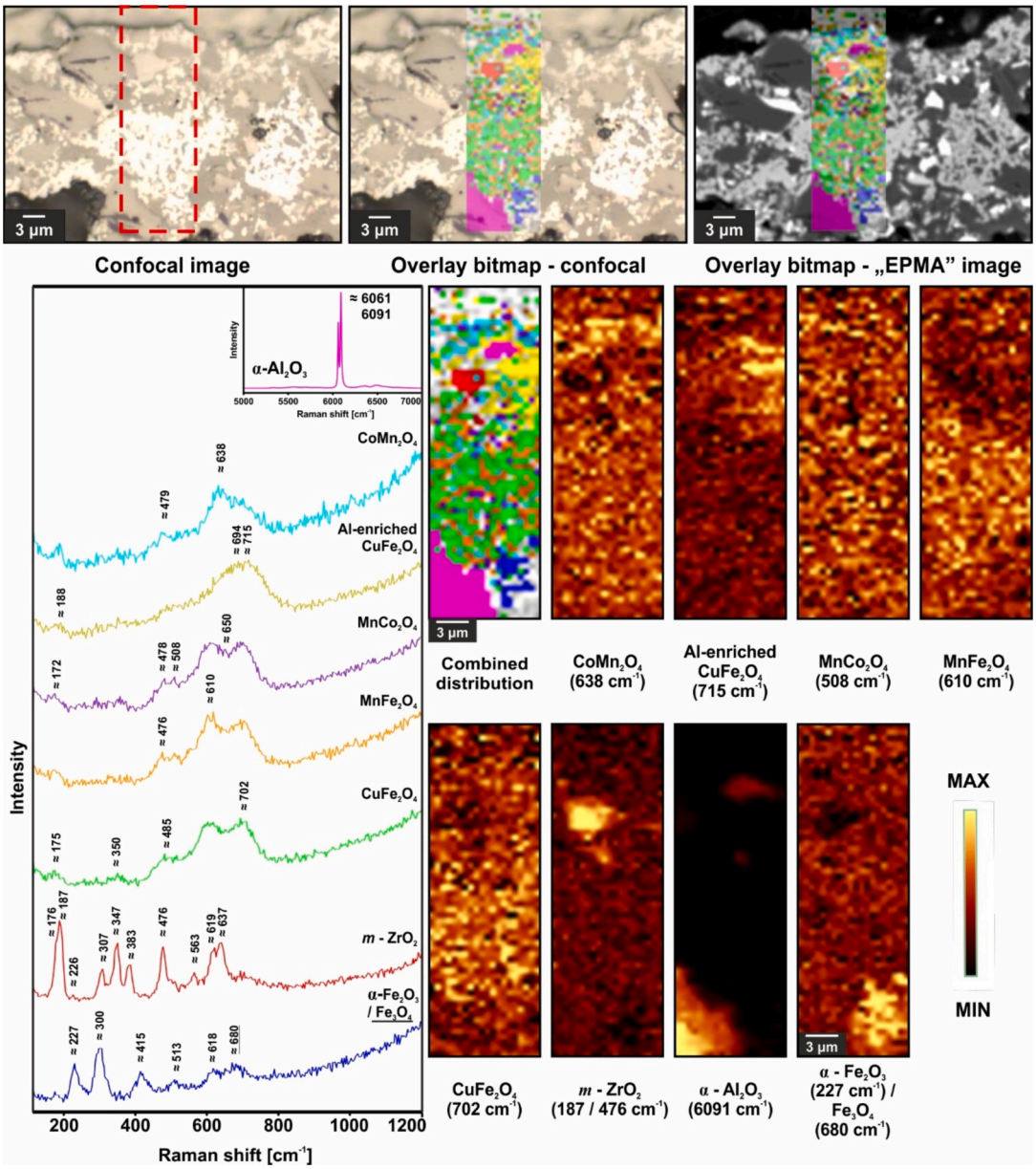

Fig. 5. Raman confocal imaging of the CIE coating after heat-treatment.

[43,44]. The combined distribution image reveals the highest share of $CuFe_2O_4$ among these three spinel phases, which is in good agreement with the EPMA mapping analysis (Fig. 2.b) and point analyses (see spots 2 and 3 for the CIE coating in Table 3) from different regions comprising a higher Cu concentration compared to Mn and Co.

For the DFI coating (Fig. 5), only one coating constituent was revealed ($CuCr_2O_4$ spinel) – it is represented by four bands (446, 480, 520 and 693 cm^{-1} as the most characteristic) [54]). Since for this type of coating only an ambient temperature manufacturing process with no additional heat treatment was undertaken, no chemical changes were observed in the microstructure, in good agreement with the EPMA mapping analysis (Fig. 2.c).

3.3. Microstructural changes during thermocyclic exposure

The microstructural changes of the coated particles were investigated after thermocyclic exposure. For better visibility of the results, the findings after 900 h exposure are presented in the Appendix (BSE images and elemental distribution maps in Fig. 12 and spot analyses in Table 5).

Table 4
Elemental concentrations determined using EPMA spot measurements by WDX from representative spots from the investigated coatings (shown in Fig. 6) after 3000 h of thermocyclic exposure at 1000 °C.

Coating	Spot no.	Concentration (at.%)							
		Fe	Mn	Cu	Al	Si	Cr	Co	O
DLR	1	20.9	5.6	7.5	9.1	0.3	–	–	55.0
	2	35.7	1.3	0.3	3.4	–	–	–	57.6
	3	20.6	5.6	7.4	8.9	–	–	–	54.9
CIE	1	11.5	2.1	3.4	5.8	4.4	–	1.4	63.3
	2	19.2	3.4	5.8	10.0	–	–	2.3	55.7
	3	20.2	3.4	6.0	10.2	–	–	2.3	55.0
DFI	1	12.1	0.3	4.7	12.9	–	5.9	–	56.1
	2	10.9	0.3	4.7	14.0	0.2	6.4	–	55.3
	3	15.6	0.3	5.5	7.2	0.1	8.8	–	54.9

These results have been taken into consideration in the discussion, together with the findings after 3000 h presented in the following.

Fig. 6 illustrates the cross-sectional BSE images and EPMA elemental

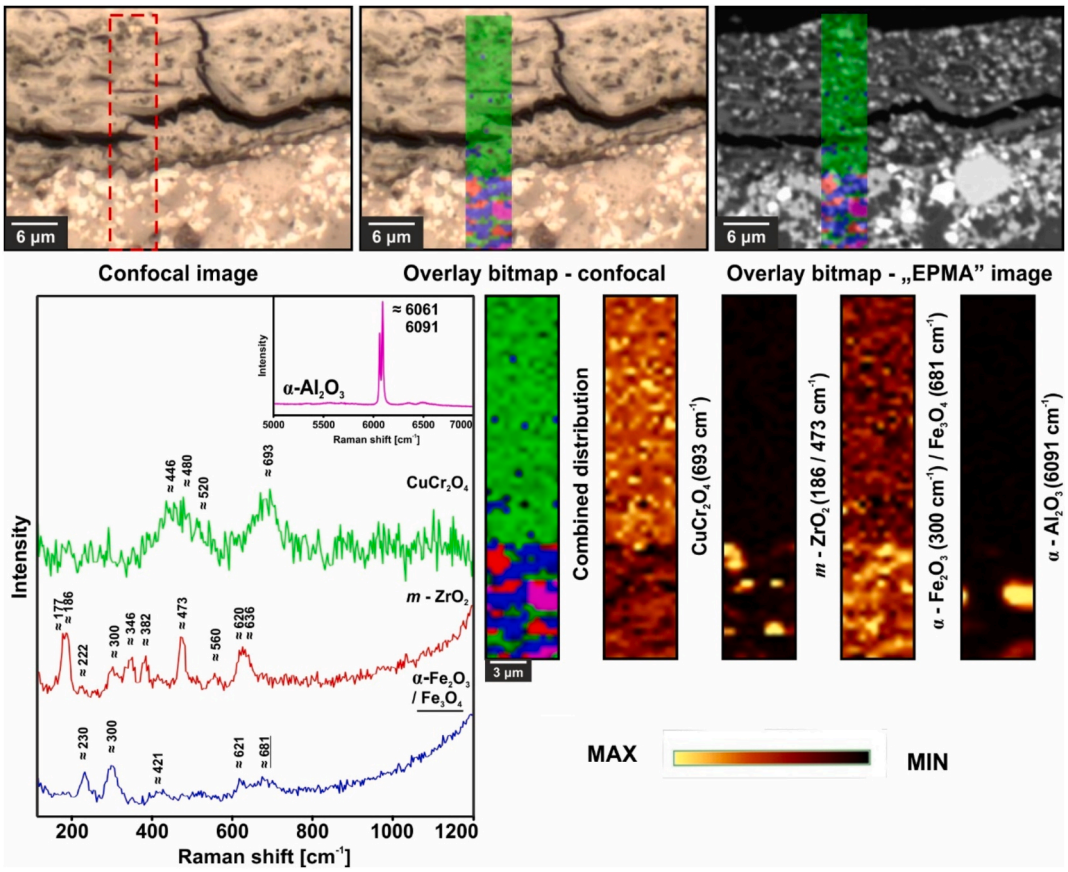

Fig. 6. Raman confocal imaging of the as-deposited DFI coating.

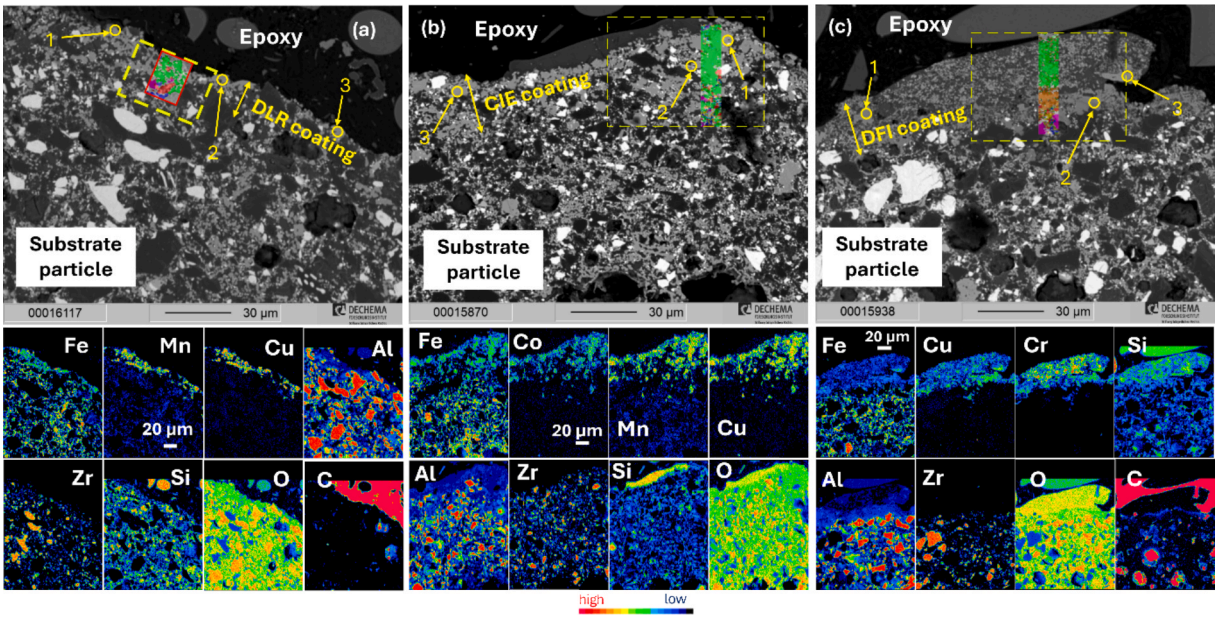

Fig. 7. Cross-sectional BSE images of (a) DLR, (b) CIE, and (c) DFI coatings deposited on substrate particles after thermocyclic exposure (3 h cycles) at 1000 °C for 3000 h. Yellow circles mark representative spots selected for WDX compositional analysis (refer to Table 4). The regions used for co-localized Raman confocal imaging (dashed yellow frame) and Raman spectroscopy (red dashed frame, embedded within the yellow frame in (b) and (c)) are also indicated. Corresponding EPMA elemental distribution maps are shown below each BSE image.

distribution maps after 3000 h of thermocyclic exposure at 1000 °C. The thickness of all coatings did not change significantly compared to the initial condition. For the DLR coating, the enrichment of the coating constituents, Cu, Mn and Fe, was maintained at the particle surface after exposure (Fig. 6.a). In addition to this, Al-enrichment, which was readily observed after the heat treatment (Fig. 3), progressed during the

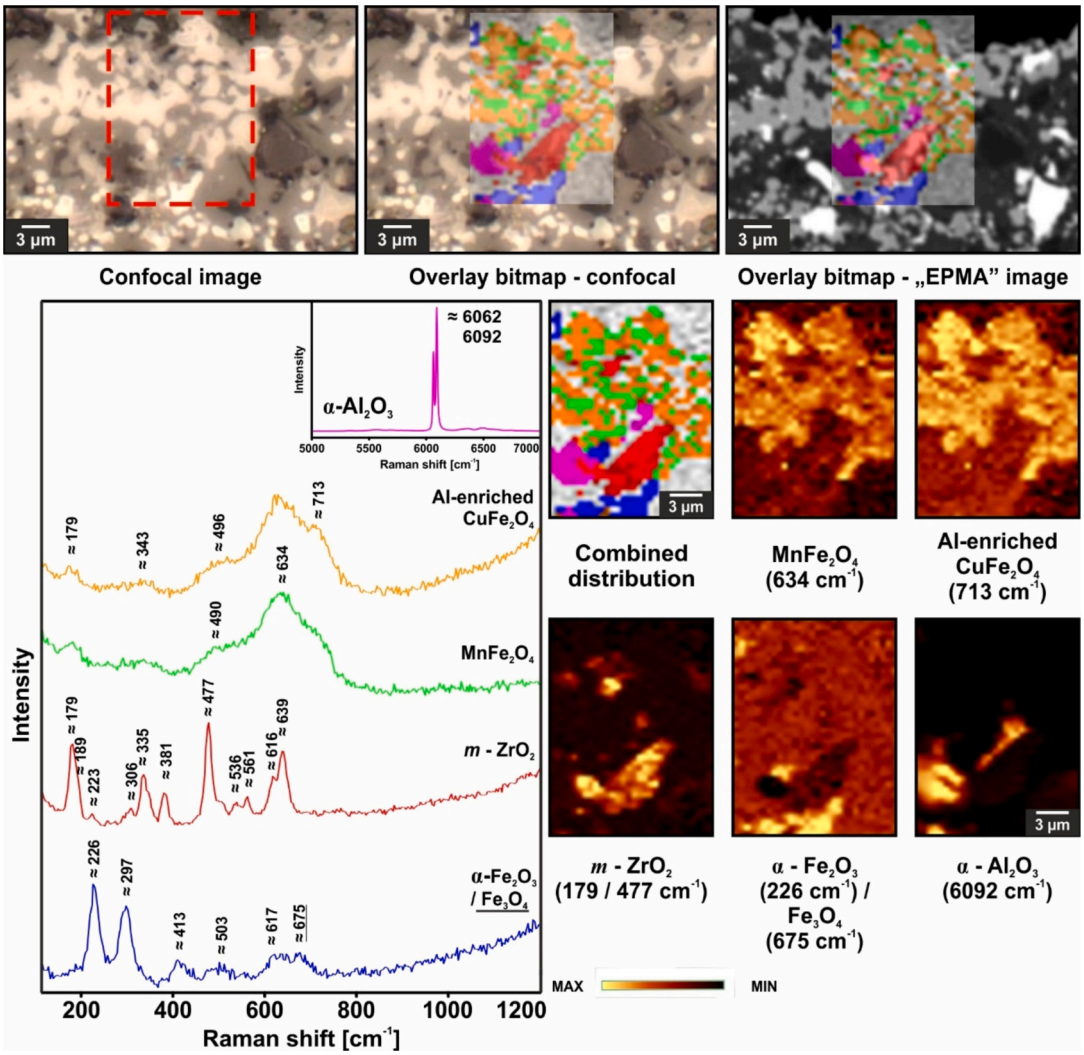

Fig. 8. Raman confocal imaging of the DLR coating after thermocyclic exposure at 1000 °C for 3000 h.

exposure (Table 4). Similarly, for the CIE coating, besides Mn, Co and Cu (coating elements), Fe- and Al-enrichment in the coating can be detected. Al-concentration in the inner layers of the CIE coating reached 10 at. % (Table 4), verifying the progressing Al-enrichment within the coating over time (see Table 3 for initial values). The Si-rich region at the surface of the coating probably originated from the addition of silica nanoparticles in the precursor solution used to manufacture the CIE coating as described in [37]. Almost analogous to the other coatings, the DFI coating also became enriched with substrate elements over time, predominantly in Fe and Al (compare Table 4 with Table 3).

Raman imaging of the DLR coating (Fig. 7) revealed that the entire coating is composed of a homogenous mixture of Al-enriched $CuFe_2O_4$ and $MnFe_2O_4$ spinels, as a result of $Cu^{2+} \leftrightarrow Mn^{3+}$ cationic exchange. Both phases are represented by very similar spectra to those before the oxidation (see Fig. 3). These results are in good agreement with the EPMA mapping analysis (Fig. 6.a) and the WDX spot analysis demonstrating the unifiorm Cu/Mn ratio concentration (see for instance, spots 1 and 3 in Table 4) across the entire coating thickness. Additionally, the combined distribution image shows slightly higher signal intensity for the Al-enriched $CuFe_2O_4$, which is in line with spot analyses proving higher Cu- than Mn-concentrations. Additionally, the band coming from $MnFe_2O_4$ broadened considerably after oxidation studies (compared to the Raman spectrum in Fig. 3 before exposure), which indicates the disorder in the structure of $MnFe_2O_4$ as a consequence of diffusion processes [55]. Regarding the substrate particles, for all investigated coating systems the initial microstructure of the particles was maintained after 3000 h of thermocyclic exposure.

Similar to the DLR coating, the CIE coating also exhibited microstructural changes after exposure (see Raman imaging in Fig. 8). Firstly, the top part of the coating changes composition to $CuMn_2O_4$ instead of $CoMn_2O_4$ (compare with Fig. 4) as represented by the spectrum with three bands (174, 540 – the most characteristic, and 630 cm^{-1}) [56]. The next and the most dominant coating constituent revealed five Raman modes at around 182, 330, 490, 651, and 705 cm^{-1} that can be assigned to Mn,Co-enriched $CuFe_2O_4$ spinel. The bands at approx. 182, 490 and 705 cm^{-1} (the most characteristic) can unequivocally be attributed to $CuFe_2O_4$ spinel [43,44], whereas the band at approx. 651 cm^{-1} comes from MnO_6 octahedral units [56,57] – in this case one can observe so-called two-mode behavior [46] in the Raman spectrum, as two distinctive modes coming from two types of octahedral units (MnO_6 and FeO_6) are visible. Furthermore, the E_g band at approx. 330 cm^{-1} is considerably shifted towards the lower Raman shift values compared to pure $CuFe_2O_4$, suggesting its enrichment in Co^{2+} cations [44], hence the final notation – Mn,Co-enriched $CuFe_2O_4$ spinel. One can also see that the band at approx. 705 cm^{-1} is already shifted towards higher Raman shift values, suggesting the presence of Al^{3+} cations across the entire coating thickness in line with EPMA mapping (Fig. 6.b) and point analyses (Table 4). In the inner region, two constituents with a lower fraction were revealed. The first one, Mn,Co,Al-enriched $CuFe_2O_4$ spinel is a derivative of the initially Al-enriched $CuFe_2O_4$ spinel (see Fig. 4), and is

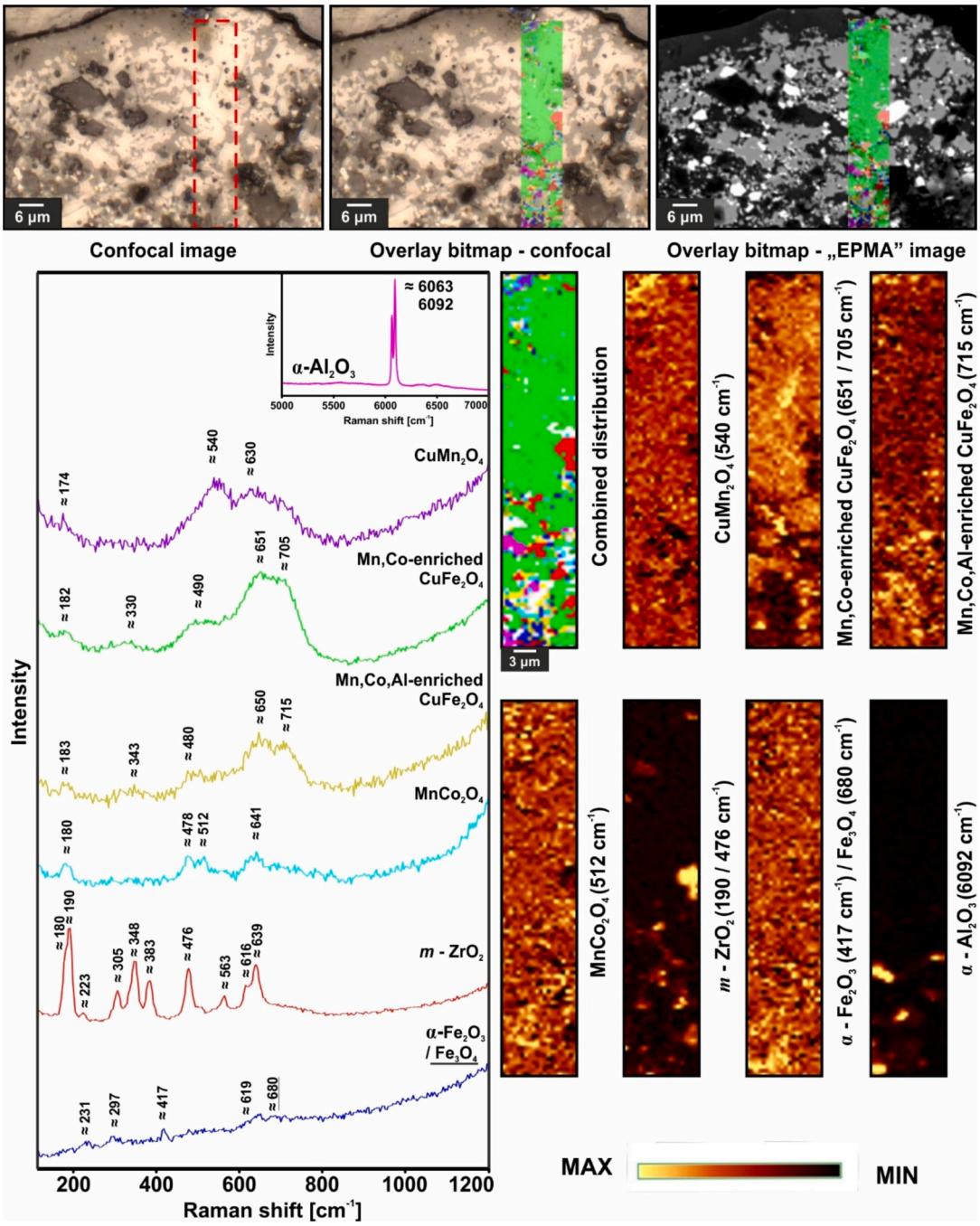

Fig. 9. Raman confocal imaging of the CIE coating after thermocyclic exposure at 1000 °C for 3000 h.

represented by a very similar spectrum to the aforementioned Mn,Co-enriched $CuFe_2O_4$ spinel present after oxidation, with two important differences – an even larger shift of the A_{1g} band towards higher Raman shift values (715 cm^{-1}) coming from AlO_6 octahedral units [47] and the shift of the $T_{2(g)2}$ band of $CuFe_2O_4$ towards lower values (480 cm^{-1}) suggesting an even higher enrichment in Co^{2+} cations [44]. The second constituent is $MnCo_2O_4$ represented by the spectrum with four typical bands at approx. 180, 478, 512 and 641 cm^{-1} (the most characteristic) [53]. Its distribution image shows traces in the top part of the coating, possibly as a derivative of $CoMn_2O_4$ spinel. A band at approx. 610 cm^{-1} disappeared which was assigned to $MnFe_2O_4$ spinel, noticeable for the coating after heat-treatment (see Fig. 4). Mn^{3+} cations present initially in $MnFe_2O_4$ can be observed on octahedral positions in $CuFe_2O_4$ spinel (as well as partially in $MnCo_2O_4$), whereas Co^{2+} cations initially present in $CoMn_2O_4$ and $MnCo_2O_4$ spinels were partially exchanged for Cu^{2+} from $CuFe_2O_4$ spinel. Such changes are in good agreement with the EPMA mapping (compare Fig. 2.b with Fig. 6.b) and WDX spot analyses (compare results for the CIE coating in Table 3 with those in Table 4) showing a more homogenized composition after thermocyclic exposure.

After exposure, Raman imaging of the DFI coating revealed three different regions along the coating thickness (Fig. 9). The outermost layer of the coating consisted predominantly of the Fe,Mn-enriched $CuCr_2O_4$ spinel, which is represented by a spectrum with two bands at approx. 527 and 686 cm^{-1}. Fe and Mn enrichment is supported by the shift of the main A_{1g} band towards lower Raman shift values (693 → 686 cm^{-1}) and the disappearance of bands at around 440–500 cm^{-1} together with the occurrence of the very broad band at approx. 527 cm^{-1} [54]. The inner zone of the coating was comprised mainly of a mixture of Fe,

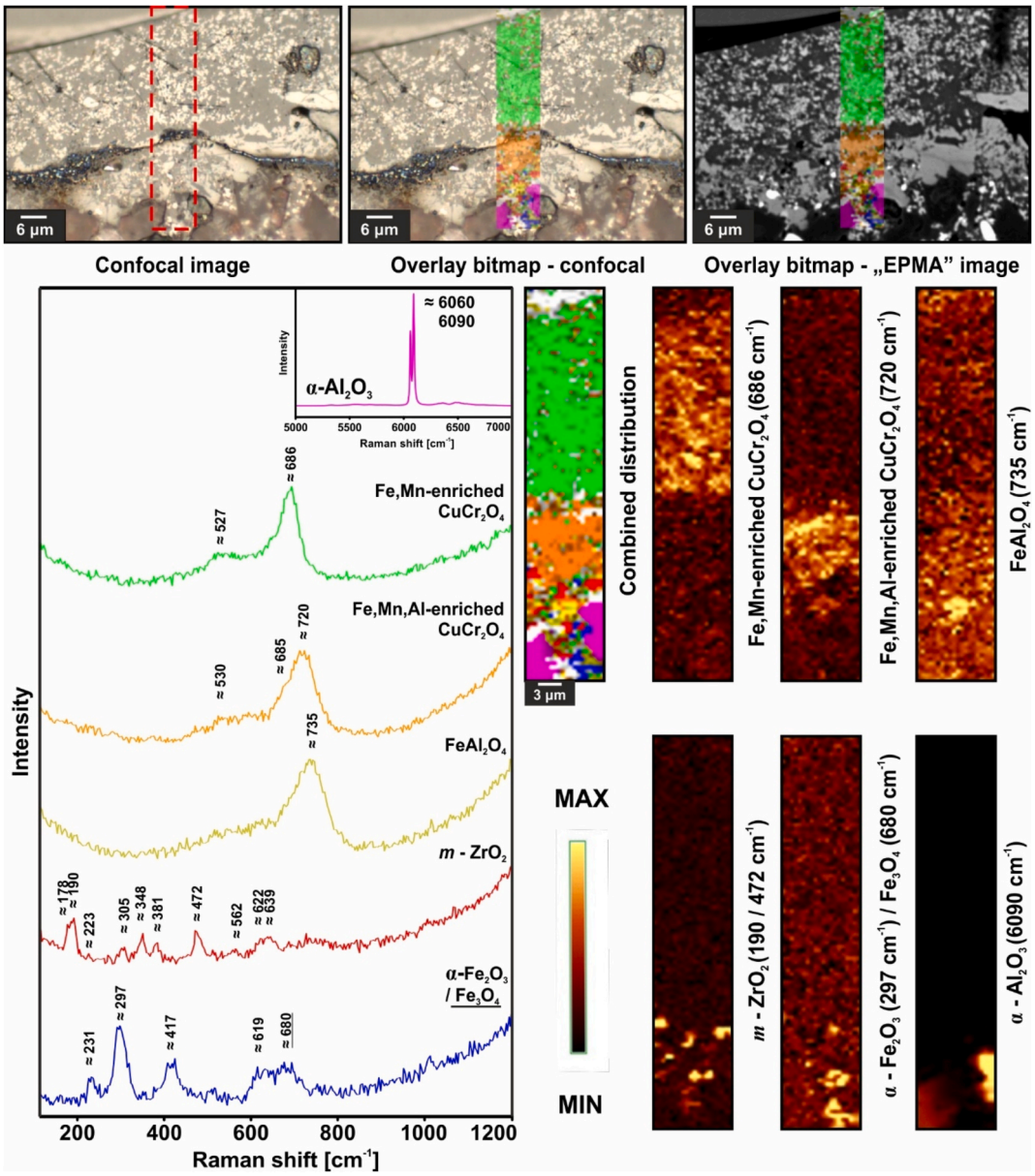

Fig. 10. Raman confocal imaging of the DFI coating after thermocyclic exposure at 1000 °C for 3000 h.

Mn,Al-enriched $CuCr_2O_4$ spinel (similar bands as above with an additional very intense band at approx. 720 cm^{-1} coming from AlO_6 octahedral units [46]) and a comparatively lower fraction of $FeAl_2O_4$ spinel represented by the spectrum with the one broad band at around 735 cm^{-1} [47]. Such compositions demonstrate the Fe and Mn enrichment (manganese possibly present in the additives, see Table 1) across the entire coating thickness (Fe^{3+} and Mn^{3+} cations substituting Cr^{3+} in [CrO_6] octahedral units [54]) coupled with significant Al-enrichment in the inner layer of the coating. These findings are in line with the elemental distribution maps (Fig. 6.c) and WDX spot analyses (Table 4) displaying the substantial enrichment of Fe and Al in the coating, together with Mn to a lower extent, as compared to the initial condition (Table 3).

4. Discussion

All of the different coatings investigated in this work consist of spinel phases that possess very high solar absorptance reaching (for the CIE coating) or even surpassing 97 % (for the DFI coating) in their as-manufactured condition (Fig. 1). Such high absorptance values are consistent with the literature studies for spinel coatings, e.g., deposited on metallic [24,28,31,58] or ceramic substrates [17,35–37,59]. The DFI and CIE coatings more or less maintained their high solar absorptance over time during thermocyclic exposure tests at 1000 °C for up to 3000 h. The DLR coating having a lower initial absorptance showed an increase in the early stages of exposure followed by stable behavior (see Fig. 1.d). These findings are in clear contrast to other investigations from literature reporting a degradation over time for spinel coatings with high solar absorptance due to the interdiffusion with the substrate and the consequential formation of new spinel solid solutions at the expense of the original spinel phase [34,60,61].

The DFI coating in the initial condition was the purest binary coating, as it was manufactured via ambient curing following the coating deposition. In the initial state, this single-layer coating predominantly consisted of $CuCr_2O_4$ spinel (Fig. 2.c and Fig. 5). While the chromite spinel was maintained after thermocyclic exposure, the coating transformed into a two-layer morphology with the outer layer showing Fe and Mn enrichment of the chromite spinel structure and the

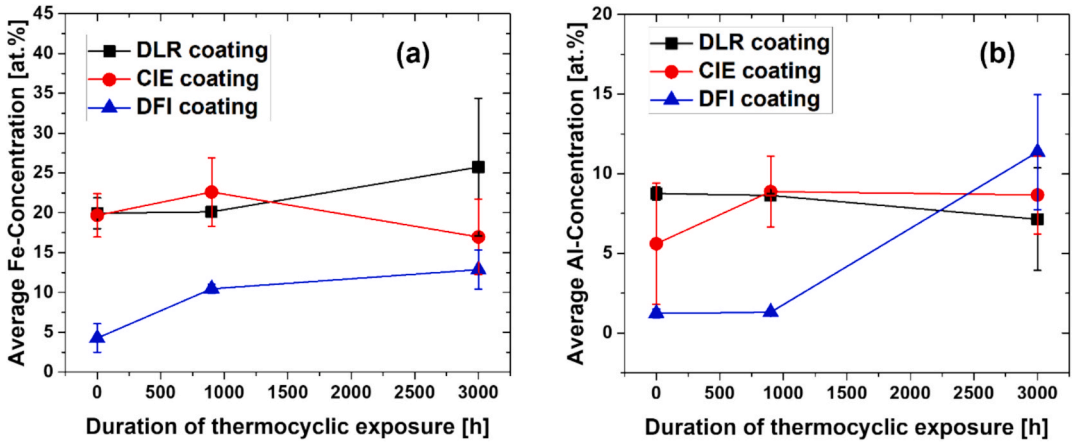

Fig. 11. Average (a) Fe- and (b) Al-concentration as a function of exposure duration in the investigated coatings determined via WDX point analyses from the representative spots shown in Fig. 2, Fig. 6 and Fig. 12 (see Appendix).

inner layer showing Al-enrichment besides Fe and Mn (Fig. 6.c and Fig. 9). A strong enrichment of the main substrate cations, Fe and Al, exceeding 10 at.% after 3000 h (average value from spot analyses, Fig. 10) was observed. Despite the limitations of spot analyses leading to these average values and a large deviation (especially for Al), the findings were consistent with the Raman mapping. Mn was enriched up to 0.3 at.% despite its absence in the initial coating (Table 3). Much less Mn was found than Fe and Al (Table 4), which is consistent with its lower amount in the substrate particles (referred to as "others" in Table 1). The enrichment of Fe, Al, and to a lower extent Mn in the chromite spinel did not affect the Cu concentration and was found to occur at the expense of Cr (see Fig. 11.c), as all these trivalent cations evidently substituted Cr^{3+} in [CrO_6] octahedral units. The effect of doping on the optical properties of the p-type semiconductor $CuCr_2O_4$ has been investigated for bulk samples. While bearing in mind that the coating-substrate interaction and the resulting substrate cation enrichment in the DFI coating occurs over time, such studies can provide valuable insights for the interpretation of the coating behavior. For instance, Bai et al. investigated the influence of Fe- and Mn-doping on the reflectance of copper chromite pigments prepared by co-precipitation [54]. They reported a higher absorptance in the UV–visible region and a higher NIR reflectance for Fe- and Mn-containing compositions. The former was attributed to a decrease in the band gap and the latter to the reduction of the free carrier concentration for doped compositions. Their findings are in line with the reflectance increase in the NIR region for the DFI coating, especially after 3000 h (Fig. 1.c). Similarly, Youn et al. studied the optical properties of $CuCr_2O_4$ pigments doped by Al, Co, Mn, Ni, Sn and Zn prepared via co-precipitation synthesis [29]. They reported a negative effect by Al, whereas the highest absorptance of around 98.7 % was found for the Mn-doped composition due to the significant reduction of the band gap. Thereafter the Mn-composition was varied at the expense of chromium in the $CuCr_{2-x}Mn_xO_4$ spinel within the range between ($0.1 \leq x \leq 1.9$) and showed an increase in the absorptance of the chromite even at the lowest dopant concentration. In the case here, this doping effect happens over time and Mn was enriched in the DFI coating after exposure together with Fe and Al (see Fig. 9). While Fe- and Mn-enrichments increase the solar absorptance by decreasing the band gap, Al incorporation is generating the opposite effect. This can explain the stable absorptance behavior of the DFI coating during thermocyclic exposure. The enrichment of Fe- and Mn to a lower content presumably counteracted the negative influence by Al in the chromite spinel, which was also predominantly found in the inner zone of the coating and not on the surface, yielding the sustained α_s value around 97 % even after 3000 h at 1000 °C.

The CIE coating exhibited a more complex structure consisting of several spinel phases in the initial condition as compared to the DFI coating (compare Fig. 4 with Fig. 5). This is associated with the spinel phase bearing three cations ($CuCoMnO_x$ general structure) and the additional heat treatment step which evidently led to cation exchange with the substrate. This can best be observed by the enrichment of substrate elements, mainly Fe and Al in the coating (Fig. 10) which resulted in a coating of different spinel phases, namely, $CoMn_2O_4$, $MnCo_2O_4$, $MnFe_2O_4$ and $CuFe_2O_4$ (Fig. 4). While Fe was enriched up to a concentration of around 20 at.% after heat-treatment, Al was enriched to a lower degree and was mainly found in the copper ferrite spinel. After exposure, the coating predominantly consisted of Mn,Co-enriched $CuFe_2O_4$, whereas the fractions of the other spinels decreased significantly (see Fig. 8). Unlike the DFI coating, the enrichment of substrate cations during thermocyclic exposure was very limited (considering the fewer composition measurements and high standard deviation) for the CIE coating (Fig. 10). This can be explained by the initial heat-treatment creating a more homogenized interface. The concentrations of the original spinel constituents over time revealed a slightly decreasing Mn- and Cu-content, whereas the Co-content remained more or less constant showing the slow, but steady homogenization of the coating during exposure (Fig. 11.b). This Mn- and Co-depletion is very small, compared to the much stronger reduction of the Cr-concentration in the DFI coating (Fig. 11.c). Yet, the formation of a more homogeneous coating mainly consisting of Mn,Co-enriched $CuFe_2O_4$ can be best explained by the cation transfer between the spinel phases in the coating during exposure. Evidently, Mn^{3+} and Co^{2+} cations were incorporated in the ferrite spinel leading to the loss of the manganite and cobaltite spinels in the coating microstructure. This can be best observed in the Raman maps showing the local presence of these spinel phases concentrated at the outermost layer or at the coating/substrate interface (Fig. 8).

Similar to $CuCr_2O_4$, the doping effects on the optical properties of $CuFe_2O_4$ have been studied in the literature for bulk specimens. Hammad et al. investigated the influence of Co-doping with bulk compositions of $Cu_{1-x}Co_xFe_2O_4$ and reported an increase in the absorptance for higher Co-substituted concentrations as a result of the reduction of band gap [62]. The effect of Mn-substitution on the structural, optical and magnetic properties of Mn-substituted $Cu_{1-x}Mn_xFe_2O_4$ was studied by Dhiwahar and co-authors. They reported a higher energy gap for increasing dopant content [63]. Contrary to the positive effect of Mn on the absorptance of $CuCr_2O_4$ (for the DFI coating), Mn incorporation in the $CuFe_2O_4$ for the CIE coating may have adversely affected the

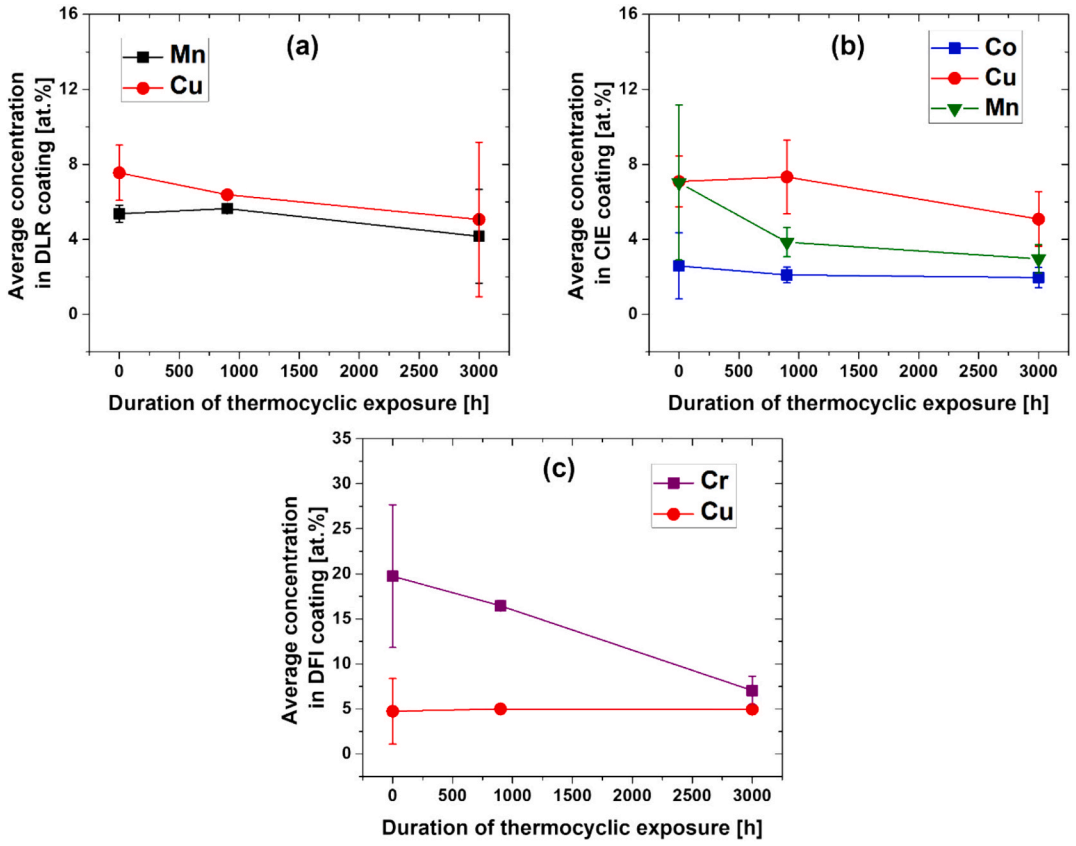

Fig. 12. Average concentration of spinel constituent elements in the investigated coatings as a function of exposure duration determined via WDX point analyses from the representative spots shown in Fig. 2, Fig. 6 and Fig. 12 (see Appendix).

absorptance. Nevertheless, the CIE coating showed a highly stable absorptance even after 3000 h of exposure (Fig. 1) despite showing significant microstructural changes. This can be associated with the positive influence of the Co-doping counteracting the adverse Mn-doping in the $CuFe_2O_4$ spinel.

The DLR coating consists of two spinel phases in the initial state, $MnFe_2O_4$ and Al-enriched $CuFe_2O_4$ (Fig. 3). The enrichment of Al in the ferrite spinel can, analogous to the CIE coating, be explained by the applied heat-treatment. However, the level of Al-enrichment was notably higher in the case of the DLR coating (see Table 3 and Fig. 10.b). This can be attributed to the higher thermal activation for diffusion by the higher heat treatment temperature (1200 °C compared to 1000 °C for CIE coating). Disregarding the high standard deviation in the spot measurements, the Fe-content of the DLR coating only slightly increased over time which can be explained by the homogenized composition after heat-treatment (Fig. 10.a). The same can also be postulated for Al, as its content only slightly decreased with progressing exposure (Fig. 10.b). The trend was similar for Cu and Mn, both showing a slight decrease over time (Fig. 11.a), which could have been affected by the aforementioned EPMA limitations and small number of spots. Yet, like the CIE coating, the cation transfer between the spinel phases present in the DLR coating resulted in microstructural changes. After exposure, the DLR coating contained the two spinels $MnFe_2O_4$ and Al-enriched $CuFe_2O_4$, however, the fraction of the copper ferrite increased over time (compare Fig. 7 with Fig. 3). The intentional incorporation of Al into Cu-Mn-Fe spinel-based coatings deposited on ceramic particles has been investigated and revealed the positive effect of Al on the absorptance of such coatings in Ref. [59]. The authors reported the formation of a coating consisting of Cu-Al rich and Fe-Mn rich regions, which have been characterized within this study as the manganese ferrite and Al-enriched copper ferrite spinels. In the $CuFe_2O_4$ spinel, Al^{3+} cations substitute for Fe^{3+} cations thereby leading to a reduction of the lattice parameter [64]. Chavan et al. investigated such a substitution in $NiAl_xFe_{2-x}O_4$ for increasing Al^{3+} substitution and reported a decrease in the optical band gap for higher Al-content in the ferrite spinel [65]. The higher fraction of the Al^{3+}-substituted ferrite spinel can explain the increase in the absorptance of the DLR coating (see Fig. 1).

Based on these findings, it can be summarized that Al^{3+}-incorporation into different spinel phases can have a mixed effect on their solar-weighted absorptance in a similar manner as for Mn^{3+}. In the case of the DFI coating, its enrichment in the chromite spinel and the consequential increase in the optical band gap was possibly counteracted by the positive effects of Mn and Fe. In the case of the DLR coating, the incorporation of Al^{3+} into the ferrite spinel evidently had a positive effect on solar-weighted absorptance. Moreover, it is worth noting that the increase in the absorptance of the DLR coating was mostly happening during the initial 900 h of exposure followed by a stable trend for up to 3000 h. This supports the hypothesis that interdiffusion with the ceramic particles and the cation exchange between the coating constituent spinel phases control the optical behavior of the coatings investigated in this study. As the driving force for these processes diminish over time due to the homogenization of concentration gradients and phase stability, a steady-state regime is reached with respect to absorptance which is then controlled by the effects of cation substitution in different spinel phases counteracting each other in terms of optical behavior.

All coatings showed high absorptance values with stable behavior despite harsh thermocyclic conditions for up to 3000 h at 1000 °C. Another promising aspect for their utilization can be their high adherence to the substrate despite the thermally induced stresses. Correspondingly, from low magnification BSE-images (exemplarily shown for the CIE coating in Fig. 13, see Appendix), no spalled regions for the coated particles were observed. This confirms the high resistance of the investigated coatings against spallation, despite the relatively high cooling rates (induced by compressed air cooling) and the possible build-up of thermally induced stresses due to the mismatch of the thermal expansion coefficient (CTE) between the spinel coating phases. The high spallation resistance of the coatings can be explained by the similar thermal expansion coefficients of the coating and substrate constituents. For instance, the CTE values for the main substrate phases, α-Al_2O_3 (7.6×10^{-6}/K [66]) and Fe_2O_3 (7.9×10^{-6}/K [67]) are similar to those of the coating phases with reported CTE values within the range of 7–9 $\times$ 10^{-6}/K for manganite and chromite spinels [68].

5. Conclusions

Three different coatings based on spinel phases with high solar absorptance deposited on Fe_2O_3-rich ceramic particles have been investigated in this study with respect to their optical properties and microstructural changes during thermocyclic exposure at 1000 °C for 3000 h. The findings can be summarized as follows:

- All three coatings showed high solar absorptance values and maintained them even after 3000 h of exposure. The DFI and CIE coatings showed almost no change in their solar absorptance around 97 %. On the contrary, while the DLR coating showed initially lower α_s values, it exhibited an increase within the first 900 h of exposure thereafter maintaining this high α_s.
- In the initial state, the DLR coatings consisted of Al-enriched $CuFe_2O_4$ and $MnFe_2O_4$, whereas the CIE coatings were comprised of $CoMn_2O_4$, $MnCo_2O_4$, $MnFe_2O_4$ and $CuFe_2O_4$. The formation of different spinel phases was associated with the heat-treatment undertaken for these coatings leading to the incorporation of substrate cations such as Fe and Al and cation substitution between the coating constituents during heat treatment. The DFI coating, manufactured via ambient curing, exhibited a microstructure consisting of the $CuCr_2O_4$ spinel.
- During thermocyclic exposure, the DFI coating revealed the enrichment of Fe, Al and Mn (to a lesser extent) from the substrate. The cationic substitution took place at the expense of Cr^{3+} and led to the formation of copper chromite doped with Fe, Al and Mn. Evidently, the negative influence of Al on increasing the optical band gap of the chromite spinel was counteracted by the positive effects of Fe and Mn, so that DFI coating maintained its high solar absorptance for exposure durations for up to 3000 h.
- The CIE coating consisted mainly of Mn,Co-enriched $CuFe_2O_4$ after exposure, whereas the fraction of other spinels decreased significantly. This was associated with the incorporation of Mn^{3+} and Co^{2+} cations in the ferrite spinel. The former had a negative influence which evidently was again counteracted by the positive effect of the latter in terms of solar absorptance showing stable behavior even after 3000 h of exposure.
- The DLR coating was comprised of $MnFe_2O_4$ and Al-enriched $CuFe_2O_4$ after exposure similar to the heat-treated condition. However, the fraction of Al-enriched copper ferrite spinel increased significantly. The increase in the solar absorptance of this coating within the first 900 h was attributed to the positive effect of Al^{3+} doping in the ferrite spinel.

6. Outlook

The coatings investigated in this study exhibited highly promising microstructural stability and optical properties for particle-based CST applications. Considering the easily applicable coating manufacturing methods can facilitate their commercialization. Their cost-efficiency (costs currently estimated using raw material prices) can be increased by process optimization and upscaling which will be investigated in the future.

The effects of the heat-treatment temperatures and durations can affect the coating microstructure significantly by the formation of different spinel phases due to the cation transfer. During operation conditions, their microstructure is governed by the cation exchange between existing spinel phases and the incorporation of substrate cations due to interdiffusion. This should be investigated in more detail in the future particularly in CST operation relevant thermocyclic conditions taking into consideration the day and night cycles to provide data for robust degradation models. Based on the findings of this study, promising spinel compositions such as Fe- and Mn-doped $CuCr_2O_4$ (based on the DFI coating), Co– and/or Al-doped $CuFe_2O_4$ (based on the CIE and DLR coatings, respectively) can provide highly promising and stable α_s values for CST applications. A further study investigating the optical behavior of such compositions is planned in the future.

CRediT authorship contribution statement

C. Oskay: Writing – review & editing, Writing – original draft, Methodology, Investigation, Formal analysis, Data curation, Conceptualization. **M. Bik:** Writing – review & editing, Writing – original draft, Methodology, Investigation, Data curation. **C. Grimme:** Writing – review & editing, Investigation. **E. White:** Writing – review & editing, Investigation. **S. Auler:** Writing – review & editing, Investigation. **M. Kerbstadt:** Writing – review & editing, Investigation. **G. Alkan:** Writing – review & editing, Methodology, Investigation, Formal analysis, Data curation. **P. Mechnich:** Writing – review & editing, Investigation. **G. San Vicente:** Writing – review & editing, Methodology, Investigation, Formal analysis, Data curation. **A. Morales:** Writing – review & editing, Methodology, Investigation, Formal analysis. **F. Sutter:** Writing – review & editing, Investigation, Data curation, Conceptualization. **D. Benitez:** Writing – review & editing, Project administration, Investigation. **A.C. González Alves:** Writing – review & editing, Investigation. **N. Benameur:** Writing – review & editing, Methodology, Investigation, Formal analysis. **S. Merlin:** Writing – review & editing, Methodology, Investigation, Formal analysis. **M. Galetz:** Writing – review & editing, Supervision, Funding acquisition, Conceptualization.

Declaration of Competing Interest

The authors declare that they have no known competing financial interests or personal relationships that could have appeared to influence the work reported in this paper.

Acknowledgements

This research was financially supported by the European Union's Horizon 2020 Research and Innovation Action (RIA) under grant agreement No. 958418 (COMPASsCO2 project). This study also received support in part from the National Science Centre (NCN) Opus project number 2023/49/B/ST11/01298 which provided funding for the Raman spectroscopy experiments. Furthermore, the authors would like to acknowledge Dr. Gerald Schmidt for conducting the EPMA measurements.

Appendix A

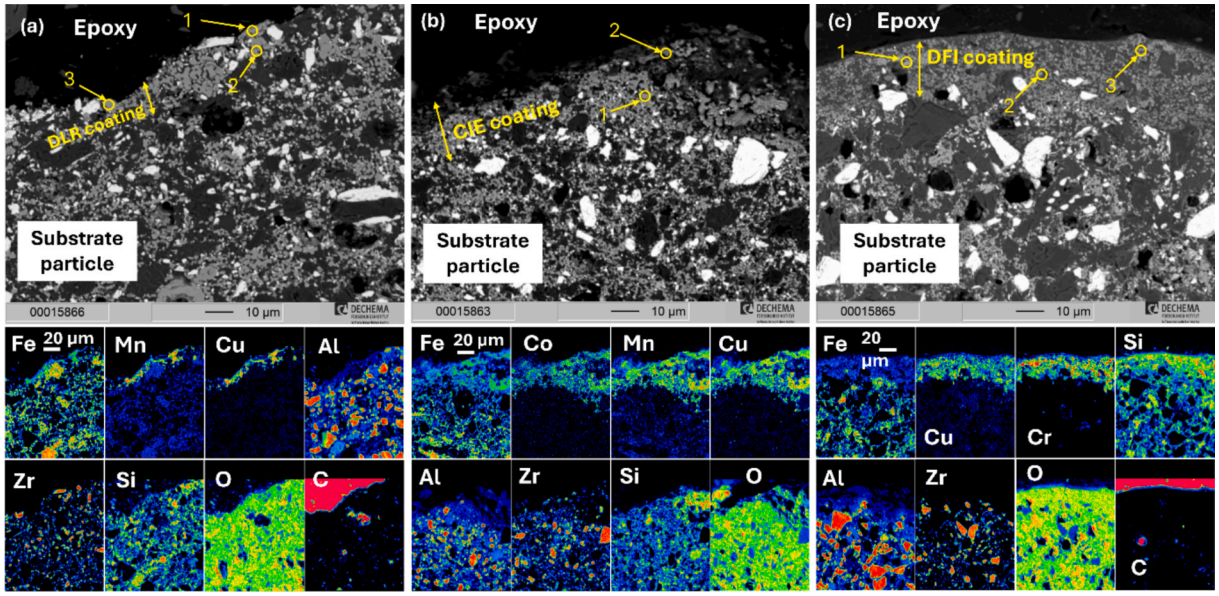

Fig. 13. Cross-sectional BSE images showing representative spots (marked with yellow circles, for the analysis see Table 5) for compositional analysis by WDX and EPMA elemental distribution maps of (a) DLR, (b) CIE and (c) DFI coatings deposited on substrate particles after thermocyclic exposure (3 h cycles) at 1000 °C for 900 h.

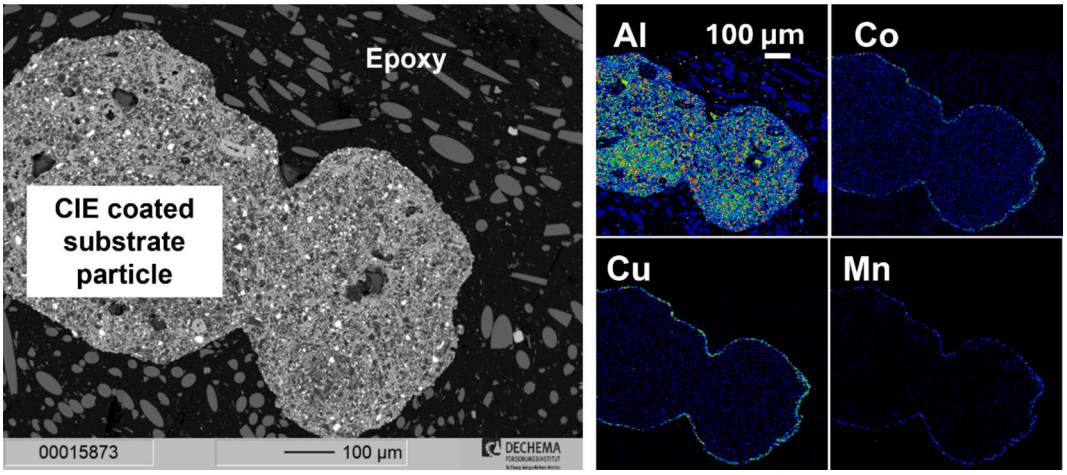

Fig. 14. Cross-sectional BSE image and EPMA elemental distribution map (for simplification only Al, Co, Cu and Mn are shown) of CIE coated substrate particles after 3000 h of thermocyclic exposure at 1000 °C emphasizing the high adherence of the coating.

Table 5
Elemental concentrations determined using EPMA spot measurements by WDX from representative spots from the investigated coatings (Fig. 10) after 900 h of thermocyclic exposure at 1000 °C.

Coating	Spot no.	Concentration (at.%)							
		Fe	Mn	Cu	Al	Si	Cr	Co	O
DLR	1	19.6	5.6	6.5	8.6	–	–	–	56.0
	2	20.8	5.6	6.2	8.8	0.2	–	–	56.1
	3	20.1	5.7	6.4	8.6	–	–	–	56.3
CIE	1	19.6	3.3	5.9	10.5	0.1	–	1.8	56.1
	2	25.7	4.4	8.7	7.3	0.6	–	2.4	49.8
DFI	1	11.1	0.3	5.4	1.2	1.3	16.9	–	57.1
	2	10.0	0.3	4.9	1.4	1.5	16.7	–	56.7
	3	10.3	0.3	4.7	1.3	2.4	15.8	–	56.0

References

[1] V. Nunes, C.S. Queirós, M. Lourenço, et al., Molten salts as engineering fluids – A review, Appl. Energy 183 (2016) 603–611.
[2] K. Vignarooban, X. Xu, A. Arvay, et al., Heat transfer fluids for concentrating solar power systems – A review, Appl. Energy 146 (2015) 383–396.
[3] C.S. Turchi, J. Vidal, M. Bauer, Molten salt power towers operating at 600–650 °C: Salt selection and cost benefits, Sol. Energy 164 (2018) 38–46.
[4] J.I. Linares, M.J. Montes, A. Cantizano, et al., A novel supercritical CO2 recompression Brayton power cycle for power tower concentrating solar plants, Appl. Energy 263 (2020) 114644.
[5] C. Prieto, S. Fereres, F.J. Ruiz-Cabañas, et al., Carbonate molten salt solar thermal pilot facility: Plant design, commissioning and operation up to 700 °C, Renew. Energy 151 (2020) 528–541.
[6] B. Grégoire, C. Oskay, T.M. Meißner, et al., Corrosion mechanisms of ferritic-martensitic P91 steel and Inconel 600 nickel-based alloy in molten chlorides. Part II: NaCl-KCl-MgCl2 ternary system, Sol. Energy Mater. Sol. Cells 216 (2020) 110675.
[7] J. Martin and V. Jr, ASCUAS: a solar central receiver utilizing a solid thermal carrier, Sandia National Lab. (SNL-CA), Livermore, CA (United States), SAND82-8203, 1982, https://www.osti.gov/biblio/5663779.
[8] C.K. Ho, A review of high-temperature particle receivers for concentrating solar power, Appl. Therm. Eng. 109 (2016) 958–969.
[9] M. Fernández-Torrijos, K.J. Albrecht, C.K. Ho, Dynamic modeling of a particle/supercritical CO2 heat exchanger for transient analysis and control, Appl. Energy 226 (2018) 595–606.
[10] C. K. Ho, T. Conboy, J. Ortega et al., High-Temperature Receiver Designs for Supercritical CO2 Closed-Loop Brayton Cycles, in Proceedings of the ASME 8th International Conference on Energy Sustainability - 2014: Presented at ASME 2014 8th International Conference on Energy Sustainability; June 30 - July 2, 2014, Boston, Massachusetts, USA, ASME, New York, NY, 2014.
[11] K. Jiang, X. Du, Y. Kong, et al., A comprehensive review on solid particle receivers of concentrated solar power, Renew. Sustain. Energy Rev. 116 (2019) 109463.
[12] T. Baumann, S. Zunft, Properties of granular materials as heat transfer and storage medium in CSP application, Sol. Energy Mater. Sol. Cells 143 (2015) 38–47.
[13] N. Siegel, M. Gross, C. Ho, et al., Physical Properties of Solid Particle Thermal Energy Storage Media for Concentrating Solar Power Applications, Energy Procedia 49 (2014) 1015–1023.
[14] A. Calderón, C. Barreneche, A. Palacios et al., Review of solid particle materials for heat transfer fluid and thermal energy storage in solar thermal power plants, Energy Storage, vol. 1, no. 4, 2019.
[15] B.R. Barboza, B. Chen, C. Li, A review on proppant transport modelling, J. Petrol. Sci. Eng. 204 (2021) 108753.
[16] G. Alkan, P. Mechnich, H. Barbri, et al., Evaluation of ceramic proppants as heat transfer and storage medium, AIP Conf. Proc. 2815 (2023) 160002.
[17] B. Gobereit, L. Amsbeck, C. Happich, et al., Assessment and improvement of optical properties of particles for solid particle receiver, Sol. Energy 199 (2020) 844–851.
[18] J. Roop, S. Jeter, S. I. Abdel-Khalik et al., Optical Properties of Select Particulates After High-Temperature Exposure, in Proceedings of the ASME 8th International Conference on Energy Sustainability - 2014: Presented at ASME 2014 8th International Conference on Energy Sustainability; June 30 - July 2, 2014, Boston, Massachusetts, USA, ASME, New York, NY, 2014.
[19] F. Sutter, G. Alkan, N. Benameur, et al., Thermal and environmental durability of novel particles for Concentrated solar thermal technologies, Sol. Energy Mater. Sol. Cells 281 (2025) 113316.
[20] A. Palacios, A. Calderón, C. Barreneche, et al., Study on solar absorptance and thermal stability of solid particles materials used as TES at high temperature on different aging stages for CSP applications, Sol. Energy Mater. Sol. Cells 201 (2019) 110088.
[21] G. Alkan, P. Mechnich, H. Lucas, et al., Assessment of Metallurgical Slags as Solar Heat Absorber Particles, Minerals 12 (2) (2022) 121.
[22] L. Noč, I. Jerman, Review of the spectrally selective (CSP) absorber coatings, suitable for use in SHIP, Sol. Energy Mater. Sol. Cells 238 (2022) 111625.
[23] Q.-C. Zhang, Recent progress in high-temperature solar selective coatings, Sol. Energy Mater. Sol. Cells 62 (1–2) (2000) 63–74.
[24] S. Caron, J. Garrido, E. Setien et al., Forty shades of black: A benchmark of high temperature sprayable black coatings applied on Haynes 230, in SOLARPACES 2019: International Conference on Concentrating Solar Power and Chemical Energy Systems, p. 150007, AIP Publishing, 2020.
[25] A. Boubault, C.K. Ho, A. Hall, et al., Durability of solar absorber coatings and their cost-effectiveness, Sol. Energy Mater. Sol. Cells 166 (2017) 176–184.
[26] C. K. Ho, A. R. Mahoney, A. Ambrosini et al., Characterization of Pyromark 2500 Paint for High-Temperature Solar Receivers, Journal of Solar Energy Engineering, vol. 136, no. 1, 2014.
[27] S. Hosseini, J.F. Torres, M. Taheri, et al., Stability and characterisation of Pyromark 2500 cured at different temperatures, Sol. Energy 265 (2023) 112102.
[28] D.E. Karas, J. Byun, J. Moon, et al., Copper-oxide spinel absorber coatings for high-temperature concentrated solar power systems, Sol. Energy Mater. Sol. Cells 182 (2018) 321–330.
[29] Y. Youn, J. Miller, K. Nwe, et al., Effects of Metal Dopings on CuCr 2 O 4 Pigment for Use in Concentrated Solar Power Solar Selective Coatings, ACS Appl. Energy Mater. 2 (1) (2019) 882–888.
[30] M. Dondi, C. Zanelli, M. Ardit, et al., Ni-free, black ceramic pigments based on Co—Cr—Fe—Mn spinels: A reappraisal of crystal structure, colour and technological behaviour, Ceram. Int. 39 (8) (2013) 9533–9547.
[31] R. Harzallah, M. Larnicol, C. Leclercq, et al., in: Development of high performances solar absorber coatings, AIP Publishing, 2019, p. 30026.
[32] R. Reoyo-Prats, A. Carling Plaza, O. Faugeroux, et al., Accelerated aging of absorber coatings for CSP receivers under real high solar flux – Evolution of their optical properties, Sol. Energy Mater. Sol. Cells 193 (2019) 92–100.
[33] T. M. Meißner, C. Oskay, D. Fähsing et al., Improving optical properties of diffusion-based absorber coatings for CSP tower systems, in SOLARPACES 2018: International Conference on Concentrating Solar Power and Chemical Energy Systems, p. 20003, AIP Publishing, 2019.
[34] I. Jerman, F.R. Zepeda, L. Noč, Merging of oxide species with black spinel structure by CSP operating temperature, Author(s) (2018) 220002.
[35] K.M. Chung, R. Chen, Black coating of quartz sand towards low-cost solar-absorbing and thermal energy storage material for concentrating solar power, Sol. Energy 249 (2023) 98–106.
[36] G. Alkan, P. Mechnich, J. Pernpeintner, Improved Performance of Ceramic Solar Absorber Particles Coated with Black Oxide Pigment Deposited by Resonant Acoustic Mixing and Reaction Sintering, Coatings 12 (6) (2022) 757.
[37] M. Farchado, G. San Vicente, N. Barandica et al., Performance Improvement of Csp Particle Receivers by Depositing Spinel Absorber Coatings, Solar Energy Materials and Solar Cells, no. 266, 2024.
[38] P.B. Bendix, S.K. Henninger, H.-M. Henning, Temperature and Mechanical Stabilities and Changes in Porosity of Silicone Binder Based Zeolite Coatings, Ind. Eng. Chem. Res. 55 (17) (2016) 4942–4947.
[39] "ISO 13573:2012 Test method for thermal cycling exposure testing under high temperature corrosion conditions for metallic materials,".
[40] F. Sutter, J. Pernpeintner, S. Caron et al., Method to evaluate the reflectance, absorptance and emittance of particles for concentrating solar power technology, https://elib.dlr.de/189228/.
[41] ASTM, ASTM E903-20: Test Method for Solar Absorptance, Reflectance, and Transmittance of Materials Using Integrating Spheres,".
[42] S. Caron, L. Herding, Y. Binyamin, et al., Laboratory intercomparison of solar absorptance and thermal emittance measurements at room temperature, Sol. Energy Mater. Sol. Cells 238 (2022) 111579.
[43] S. Mallesh, M. Gu, K.H. Kim, Cubic to Tetragonal Phase Transition in $CuFe_2O_4$. Experimental Details Nanoparticles, Journal of Magnetics 26 (1) (2021) 7–13.
[44] R. Dhyani, R.C. Srivastava, G. Dixit, Study of Magnetic and Temperature-Dependent Dielectric Properties of Co-CuFe2O4 Nanoferrites, J. Electron. Mater. 51 (10) (2022) 5492–5507.
[45] M.C. Galetz, C. Schlereth, E.M.H. White, et al., An Expanded Model for the Pressure Effect in Metal Dusting of Mn-Containing Alloy 600 Based on Advanced Scale Characterization, High Temp. Corros. Mater. 100 (5–6) (2023) 541–555.
[46] B.D. Hosterman, Raman Spectroscopic Study of Solid Solution Spinel Oxides, University of Nevada, Las Vegas, 2011.
[47] V. D'Ippolito, G.B. Andreozzi, D. Bersani, et al., Raman fingerprint of chromate, aluminate and ferrite spinels, J. Raman Spectrosc. 46 (12) (2015) 1255–1264.
[48] W. Wang, Z. Ding, X. Zhao et al., Microstructure and magnetic properties of MFe2O4 (M = Co, Ni, and Mn) ferrite nanocrystals prepared using colloid mill and hydrothermal method, Journal of Applied Physics, vol. 117, no. 17, 2015.
[49] S.N. Basahel, T.T. Ali, M. Mokhtar, et al., Influence of crystal structure of nanosized ZrO2 on photocatalytic degradation of methyl orange, Nanoscale Res. Lett. 10 (2015) 73.
[50] X. Wei, Y. Zhou, Y. Li, et al., Polymorphous transformation of rod-shaped iron oxides and their catalytic properties in selective reduction of NO by NH 3, RSC Adv. 5 (81) (2015) 66141–66146.
[51] H. Jiu, N. Ren, L. Jiang, et al., Hierarchical porous CoMn2O4 microspheres with sub-nanoparticles as advanced anode for high-performance lithium-ion batteries, J. Solid State Electrochem. 22 (9) (2018) 2747–2755.
[52] N. Kalita, A. Sahu, S. Bhowmick, et al., Synchronized redox pairs in metal oxide/hydroxide chemical analogues for an efficient oxygen evolution reaction, Chem. Commun. (Camb.) 58 (99) (2022) 13747–13750.
[53] G. Varga, A. Sápi, T. Varga, et al., Ambient pressure CO2 hydrogenation over a cobalt/manganese-oxide nanostructured interface: A combined in situ and ex situ study, J. Catal. 386 (2020) 70–80.
[54] M. Bai, W. Li, Y. Hong, et al., Synthesis and characterization of Fe/Mn co-doped CuCr2O4 black pigment with high near-infrared reflectance, Sol. Energy 234 (2022) 240–250.
[55] B. Lemieszek, J. Ignaczak, K. Lankauf, et al., CuMn1.7Fe0.3O4 – Me2O3 (Me=Y, Gd) Ceramic Bilayers as Protective Interconnect Coatings for Solid Oxide Cells, Corros. Sci. (2024) under revi.
[56] T. van Everbroeck, R.-G. Ciocarlan, W. van Hoey, et al., Copper-Containing Mixed Metal Oxides (Al, Fe, Mn) for Application in Three-Way Catalysis, Catalysts 10 (11) (2020) 1344.
[57] X. Yang, W. Tang, Z. Liu, et al., Synthesis of lithium-rich LixMn2O4 spinels by lithiation and heat-treatment of defective spinels, J. Mater. Chem. 12 (3) (2002) 489–495.
[58] S. Hosseini, J.F. Torres, R., Harzallah et al., Long-term thermal stability testing of the CoteRill®750 solar absorber coating, AIP Conf. Proc. 2815, 020006 (2023) 20006.
[59] G. Alkan, P. Mechnich, J. Pernpeintner, Using an Al-Incorporated Deep Black Pigment Coating to Enhance the Solar Absorptance of Iron Oxide-Rich Particles, Coatings 13 (11) (2023) 1925.
[60] A. Ambrosini, T. N. Lambert, A. Boubault et al., Thermal Stability of Oxide-Based Solar Selective Coatings for CSP Central Receivers, in Proceedings of the ASME 9th International Conference on Energy Sustainability - 2015: Presented at ASME 2015 9th International Conference on Energy Sustainability, June 28-July 2, 2015, San

Diego, California, USA, The American Society of Mechanical Engineers, New York, N.Y., 2016.
[61] A.S. Ulrich, C. Schlereth, B. Grégoire, et al., Cr–Mn-diffusion coatings on VM12: In situ spinel formation with high solar absorptance for concentrated solar plants, Sol. Energy Mater. Sol. Cells 257 (2023) 112382.
[62] T.M. Hammad, S. Kuhn, A.A. Amsha, et al., Investigation of structural, optical, and magnetic properties of Co2+ ions substituted CuFe2O4 spinel ferrite nanoparticles prepared via precipitation approach, J. Aust. Ceram. Soc. 57 (2) (2021) 543–553.
[63] A.T. Dhiwahar, S. Revathi, N.M. Basith, et al., Investigation of Visible Light Driven Photocatalytic Activity of Mn Doped CuFe2O4 Nanoparticles, J. Clust. Sci. 35 (3) (2024) 779–798.
[64] S. Rather, H.S. Bamufleh, H. Alhumade, et al., Morphological, structural, surface, thermal, chemical, and magnetic properties of Al-doped nanostructured copper ferrites, Ceram. Int. 49 (12) (2023) 20261–20272.
[65] A.R. Chavan, S.D. Birajdar, R.R. Chilwar, et al., Structural, morphological, optical, magnetic and electrical properties of Al3+ substituted nickel ferrite thin films, J. Alloy. Compd. 735 (2018) 2287–2297.
[66] S. Xuan, Y. Tian, X. Kong, et al., Enhancement of thermal shock resistance of Al2O3–MgAl2O4 composites by controlling the content and distribution of spinel phase, Ceram. Int. 49 (24) (2023) 39908–39916.
[67] Y. Fei, Thermal Expansion, in AGU Reference Shelf, American Geophysical Union, Washington, D. C., 2013, pp. 29–44.
[68] H. Ling, Electrical and Thermal Properties of Spinels, ECS Proceedings Volumes 2005–07 (1) (2005) 1866–1873.